PAPER

Check for updates

Rapid and long-lasting acceleration of zero-valent iron nanoparticles@Ti$_3$C$_2$-based MXene/peroxymonosulfate oxidation with bi-active centers toward ranitidine removal†

Yiyang Ma,[abc] Dongbin Xiong,[d] Xiaofan Lv,[e] Xuesong Zhao,[abc] Chenchen Meng,[abf] Haijiao Xie[g] and Zhenghua Zhang ![ORCID] *[abc]

Advanced oxidation processes (AOPs) can effectively degrade ranitidine, a pharmaceutical that is a typical precursor of nitrosamine dimethylamine (NDMA), an extremely potent human carcinogen. Herein, novel magnetic Ti$_3$C$_2$-based MXene nanosheets decorated with nanoscale zero-valent iron particles (nZVIPs@Ti$_3$C$_2$ nanosheets) were synthesized to boost catalytic peroxymonosulfate (PMS) activation, exhibiting remarkable reactivity and stability for the rapid removal of ranitidine under mild conditions. The response surface methodology (RSM) confirmed that the initial solution pH and PMS dosage were the main factors affecting the heterogeneous oxidation process. The long-lasting catalytic activity was mainly attributed to the rapid charge transfer between dual electron-rich active centers ($\equiv$Fe and $\equiv$Ti), with SO$_4^{\cdot-}$ and HO$^\cdot$ derived from PMS activation being responsible for ranitidine degradation, among which SO$_4^{\cdot-}$ was the major contributor. Density functional theory (DFT) calculations also confirmed that the as-synthesized nZVIPs@Ti$_3$C$_2$ nanosheets provided bi-active centers for PMS activation, and this process triggered a series of thermodynamically favorable reactions. This study demonstrates a recyclable oxidation method for the rapid removal of ranitidine, which may be applicable to the degradation of other challenging pollutants.

1. Introduction

Pharmaceuticals and personal care products (PPCPs) are a newly emerging type of organic pollutants, which have been detected at various concentrations in surface water, groundwater and soils worldwide, mainly originating from anthropogenic pollution sources.[1–3] These PPCPs, especially some of them containing dimethylamine groups in their molecular structure, have been verified as potential precursors of *N*-nitrosodimethylamine (NDMA), which presents a 10^{-6}-fold increase in lifetime cancer risk at a concentration of only 0.7 ng L^{-1}.[4] Ranitidine is a histamine H$_2$-receptor antagonist commonly used for the treatment of gastroesophageal reflux and ulcers. However, this compound is not metabolized completely by the human body and more than 70% of untransformed ranitidine may be excreted in the urine.[5] Furthermore, recent studies have demonstrated that ranitidine is a potentially potent NDMA precursor, exhibiting a high NDMA molar conversion rate of 89.9–94.2% during the decomposition process.[6,7] Therefore, since ranitidine is an emerging contaminant that has been widely introduced into the natural environment,[3,8] an effective treatment technique used to remove the compound from water is highly desired.

Heterogeneous Fenton-like oxidation is an advanced oxidation process (AOP) which has developed rapidly in the past decade, overcoming the limitations (*e.g.* the narrow pH range, high yield of chemical sludge and poor stability) of the traditional homogeneous Fenton process.[9–12] Compared with the short-lived hydrogen peroxide (H$_2$O$_2$), peroxymonosulfate (PMS, HSO$_5^-$) belongs to a chemically stable and solid oxidant with an asymmetric structure, and serves as a precursor for the generation of sulfate radicals (SO$_4^{\cdot-}$) *via* activation.[13,14] The standard redox potential of E_0(SO$_4^{\cdot-}$/SO$_4^{2-}$) (2.5–3.1 V) is higher than

[a]Institute of Environmental Engineering & Nano-Technology, Tsinghua Shenzhen International Graduate School, Tsinghua University, Shenzhen 518055, Guangdong, China. E-mail: zhenghua.zhang@sz.tsinghua.edu.cn

[b]Guangdong Provincial Engineering Research Center for Urban Water Recycling and Environmental Safety, Tsinghua Shenzhen International Graduate School, Tsinghua University, Shenzhen 518055, Guangdong, China

[c]School of Environment, Tsinghua University, Beijing 100084, China

[d]Pillar of Engineering Product Development, Singapore University of Technology and Design, Singapore 487372, Singapore

[e]Beijing Key Laboratory of Water Resources & Environmental Engineering, China University of Geosciences (Beijing), Beijing 100083, China

[f]College of Chemistry and Environmental Engineering, Shenzhen University, Shenzhen 518060, China

[g]Hangzhou Yanqu Information Technology Co., Ltd, Hangzhou 310003, China

† Electronic supplementary information (ESI) available. See DOI: 10.1039/d1ta02046c

This journal is © The Royal Society of Chemistry 2021

J. Mater. Chem. A, 2021, **9**, 19817–19833 | 19817

that of $E_0(HO^{\bullet}/OH^-)$ (2.7 V), and therefore $SO_4^{\bullet-}$ has been used as a more aggressive oxidizing agent for aqueous contaminant degradation.[15,16] Various transition metal elements such as Co, Ce, Fe and Ni have been widely applied for PMS activation (eqn (1)), due to the low energy consumption requirements of these activation systems.[17,18]

$$M^{n+} + 2HSO_5^- \rightarrow M^{(n+1)+} + SO_4^{\bullet-} + SO_4^{2-} + 2HO^{\bullet} \quad (1)$$
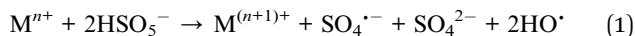
In recent years, heterogeneous Fenton-like oxidization methods utilizing nanoscale zero-valent iron particles (nZVIPs) have attracted considerable attention due to their high surface reactivity, large specific surface area and low cost, and this approach is established by replacing dissolved ferrous ions in the Fenton reagent.[19–21] However, some disadvantages of nZVIPs still greatly limited their application in water pollution treatment. When their particle size decreases to the nanometer scale, agglomeration of nZVIPs in aqueous solution was inevitable due to magnetic and van der Waals forces, which would directly result in a significant decrease in the specific surface area.[22,23] It is generally accepted that these nZVIPs exhibit a distinct core–shell structure as a result of their high surface energy, which triggers a series of reactions with environmental media, causing the formation of a passivation layer on the particle surface.[24,25] More importantly, the circulation of Fe(II)/Fe(III) was blocked during the heterogeneous Fenton-like oxidation reaction, which would also be the main reason for the passivation layer formation on the nZVIP surface.[26] Particularly for pure nZVIP samples, their catalytic activities were driven by the oxidation of nZVIPs in the inner core. Therefore, the thickness and coverage area of the passivation layer on the nZVIP surface are key factors that determine the charge and degree of mass transport.[22]

To address these technical issues, the valence state cycle of Fe(II)/Fe(III) in the reaction system can be accelerated by adding chelators or reductants to heterogeneous Fenton-like reactions induced by iron-based catalysts, resulting in the release of a large amount of soluble ferrous ions into the bulk solution.[27,28] Reported literature indicates that the use of supporting materials with large specific surface areas is a highly effective method to prevent nZVIP aggregation and improve the chemical stability of metal nanoparticles in heterogeneous oxidation reactions.[21] Recently, two-dimensional transition metal carbides/carbonitrides (*i.e.*, MXenes) have been applied in many fields since their emergence, providing low-dimensional confinement quantum effects and a unique nanosheet structure with a large specific area, hydrophilicity and electrical conductivity, along with other beneficial physical and chemical characteristics.[29,30] Among them, Ti$_3$C$_2$-based MXene has been the most widely used as the titanium element (valence states of +2, +3 and +4) in its molecular structure is metastable and could further provide reactive sites for heterogeneous oxidation reactions.[31,32] However, to the best of our knowledge, no systematic investigations have been reported on the catalytic roles of nZVIPs@Ti$_3$C$_2$ for PMS activation, especially in-depth analysis on the reaction mechanisms.

In this study, a novel magnetic compound material (nZVIPs@Ti$_3$C$_2$ nanosheets) was synthesized to rapidly remove ranitidine from aqueous solution by activating PMS to yield highly reactive oxidizing species (ROS), such as $SO_4^{\bullet-}$ and $HO^{\bullet}$. The main objectives of this study were to (1) evaluate the effects of interactive relationships between experimental parameters on the catalytic activity of the nZVIPs@Ti$_3$C$_2$ nanosheets/PMS reactive system; (2) comprehensively identify the main dominant ROS responsible for ranitidine degradation; (3) conduct theoretical analysis of the catalytic roles of nZVIPs@Ti$_3$C$_2$ nanosheets; (4) clarify the mechanism of PMS activation and the Fe(II)/Fe(III) valence cycle.

2. Materials and methods

2.1 Chemicals and reagents

All chemicals and reagents used in the preparation of catalytic materials were supplied by commercial sources without further processing, with both pure nZVIPs and Ti$_3$C$_2$-based MXene synthesized in the laboratory. Details of the above-mentioned reagents and the preparation methods for pure nZVIPs and Ti$_3$C$_2$-based MXene are described in Text S1 and Fig. S1, S2 (ESI†).

2.2 Synthesis of magnetic nZVIPs@Ti$_3$C$_2$ nanosheets

To ensure the uniformity of the lamellar structure of the synthesized nZVIPs@Ti$_3$C$_2$ nanosheets, Ti$_3$C$_2$-based MXene was pre-treated by differential screening using high-speed centrifugation (3000 rpm for 15 min and then 8000 rpm for 15 min followed by 5000 rpm for 10 min). Firstly, 0.35 g of ferrous sulfate (FeSO$_4$) and 0.35 g Ti$_3$C$_2$-based MXene were placed in a 250 mL volumetric flask, with 200 mL deionized water added to dissolve the mixture under ultrasonication for 30 min. Secondly, the obtained suspension was transferred to a 500 mL three-neck flask, continually agitated at 20 rpm and then combined with 1.14 g of sodium borohydride (NaHB$_4$) dissolved in 200 mL deionized water in a dropwise manner under a continual flow of nitrogen. When the full dosage of NaHB$_4$ was added to the mixed solution, stirring was continued for 2 h until the ferrous ions were completely reduced to zero-valent iron and the solution was black in color. The synthesis process is illustrated in Fig. 1a and the whole reaction sequence is shown in eqn (2) as follows:

$$Fe(H_2O)_6^{2+}{}_{(aq)} + 2BH_4^-{}_{(aq)} \rightarrow Fe^0{}_{(s)} + 2B(OH)_3{}_{(aq)} + 7H_{2(g)}\uparrow (2)$$
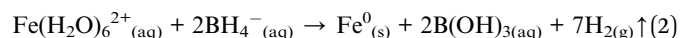
2.3 Batch experiment procedure

All degradation experiments were conducted in 200 mL glass vials sealed with a Teflon-lined cap containing 150 mL of ranitidine (10 mg L^{-1}) with constant agitation at 250 rpm, with the heterogeneous reaction initiated by the addition of 15.0 mg PMS and 11.25 mg nZVIPs@Ti$_3$C$_2$ nanosheets. The initial solution pH value was adjusted using 30 mM HCl and NaOH without buffering. At selected time intervals, 5 mL of the
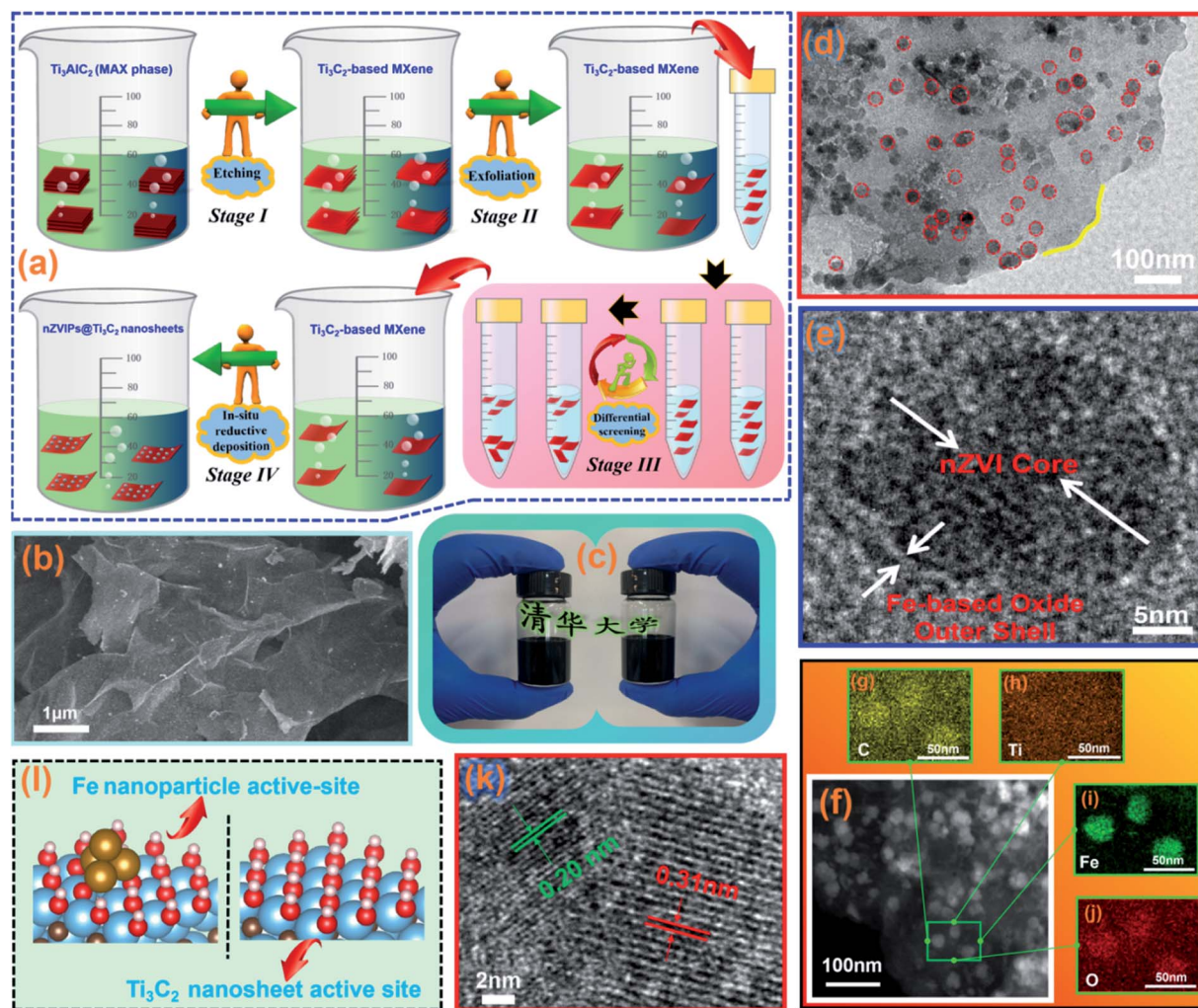
19818 | *J. Mater. Chem. A*, 2021, **9**, 19817–19833

This journal is © The Royal Society of Chemistry 2021

Fig. 1 (a) Schematic illustration of the synthesis process for nZVIPs@Ti$_3$C$_2$ nanosheets; (b) the SEM image of Ti$_3$C$_2$-based MXene powder; (c) Ti$_3$C$_2$-based MXene in aqueous solution; (d) low-magnification TEM image of nZVIPs@Ti$_3$C$_2$ nanosheets; (e) the HRTEM image of nZVIPs@Ti$_3$C$_2$ nanosheets; (f) EDS-mapping images of nZVIPs@Ti$_3$C$_2$ nanosheets including (g) carbon, (h) titanium, (i) iron and (j) oxygen elements; (k) the HRTEM image of nZVIPs@Ti$_3$C$_2$ nanosheets; (l) atomic structures of the Fe nanoparticle active-site and Ti$_3$C$_2$ nanosheet active-site. Blue, brown, gold, yellow, red, and white balls represent Ti, C, Fe, S, O, and H atoms, respectively.

aqueous sample was extracted and filtered through a 0.22 μm membrane filter, followed by the addition of a quenching agent (50 μL of sodium thiosulfate, NaS$_2$O$_3$·5H$_2$O) to remove residual radicals before High Performance Liquid Chromatography (HPLC) detection. In order to reduce the impact of experimental error, each group of experiments was carried out in parallel triplicates, with the standard deviation (SD) used to control experimental data, which was controlled within the range of ±5%. Furthermore, in ranitidine cyclic degradation tests, *in situ* consecutive experiments were conducted to avoid further oxidation of nZVIPs before the next experimental cycle.

2.4 Analytical methods

Ranitidine concentrations were analyzed using HPLC (Agilent technologies, series 1100, America) with an Eclipse XDS-C18 column (5 μm, 4.5 × 150 mm Agilent) with a mobile phase consisting of ultra-pure water and MeOH (1 : 1) at a flow rate of 1 mL min^{-1}.[33] The solution pH values were measured using

a pH meter (Thermo star-A211) and variation was controlled within a range of ±0.1. Electron paramagnetic resonance (EPR, Bruker EMX 10/12, Bremen, Germany) spectrometry was employed to identify the free radicals, with EtOH and TBA utilized as radical scavengers and DMPO applied as the spin-trapping agent for SO$_4^{\cdot-}$ and HO$^{\cdot}$. The concentrations of total iron and ferrous ions in solution during the catalytic process were measured by water quality-determination of iron-phenanthroline spectrophotometry (HJ/T 345-2007) with the procedures shown in Fig. S3 (ESI†). Density functional theory (DFT) calculations were conducted using the Vienna *Ab Initio* Package (VASP) (Text S2, ESI†). Detailed information on electrochemical measurements is provided in Text S3 (ESI†).

2.5 Materials characterization

X-ray diffraction (XRD) spectra were measured using spectrometry (D8 Advance, Bruker, Germany) in the reflection mode with Cu/Kα radiation ranging from 5° to 70° at a scanning rate

$5°$ min^{-1}. *In situ* X-ray photo-electron spectroscopy (XPS, PHI5000 VersaProbe II, Japan) was employed to record changes in surface elemental valence states. A combination of micro-laser confocal Raman spectrometry (Raman, MDTC-EQ-M15-01, France) with the wavelength of 532.05 nm of the laser source, and Fourier-transform infrared spectrometry (FTIR, Nicolet iS50, America) were used to analyze the surface chemistry components of the prepared samples. The Brunauer–Emmett–Teller (BET, ASAP2020M+C, America) system was used to evaluate the specific surface area and pore size distribution of materials. Magnetic data were recorded using a vibrating sample magnetometer (VSM, Quantum Design PPMS-9, America). The zeta potential of the prepared samples was recorded under different pH conditions using a zeta potential analyzer (Nano ZS, England). The morphology of the prepared samples was characterized by field-emission scanning electron microscopy (SEM, Hitachi SU8010, Japan), high-resolution transmission electron microscopy (HTEM, FEI Tecnai G2 F30, America) and atomic force microscopy (AFM, Bruker Dimension ICON, Germany).

3. Results and discussion

3.1 Characterization of nZVIPs@Ti$_3$C$_2$ nanosheets

Nanoscale zero-valent iron particles (nZVIPs) were well-established catalysts that are useful for water contamination remediation. However, their inherent magnetic force and high surface energy cause an inevitable significant increase in the average particle size. In order to overcome this disadvantage, Ti$_3$C$_2$-based MXene was used as a support material for nZVIPs to obtain novel physicochemical properties, including stable reactivity and nanoparticle dispersivity. Herein, the morphological and structural features of nZVIPs@Ti$_3$C$_2$ nanosheets were established using SEM, TEM and HRTEM.

As shown in Fig. 1b, the nano-scale structure characteristics of the exfoliated Ti$_3$AlC$_2$ MAX phase (*i.e.*, Ti$_3$C$_2$-based MXene) were investigated by SEM observation, and the black powder was dissolved in aqueous solution (Fig. 1c). Compared with the irregular lumpy structure of the Ti$_3$AlC$_2$ MAX phase (Fig. S4a, ESI†), the synthesized Ti$_3$C$_2$-based MXene samples exhibited ultrathin sheet structures. In addition, a necklace-like structure of the pure nZVIP sample with partial agglomeration can be observed in Fig. S4b,† and the corresponding particle sizes range from 100 to 250 nm. The SEM image of nZVIPs@Ti$_3$C$_2$ nanosheets at low-magnification as shown in Fig. S5 (ESI†), and the corresponding elemental distribution of nZVIPs@Ti$_3$C$_2$ nanosheets, including C, Ti and Fe, further established the relationship between the nZVIP distribution and Ti$_3$C$_2$-based MXene combinations. It could be observed from the TEM image that nZVIPs were uniformly immobilized on the surface of Ti$_3$C$_2$-based MXene (Fig. 1d). The actual geometric sizes of nZVIPs@Ti$_3$C$_2$ nanosheets stemming from the atomic force microscopy image as shown in Fig. S6 (ESI†) suggested that synthesized magnetic nanosheets with the thickness of around 10–30 nm were successfully obtained. These experimental results also further confirmed that nZVIPs were uniformly immobilized on the surface of the Ti$_3$C$_2$-based MXene

nanosheets. Additionally, the HRTEM image demonstrated that a large number of nZVIPs with diameters of 10–30 nm were deposited on the surface of Ti$_3$C$_2$-based MXene (Fig. 1f–j) with the corresponding atomic and weight ratios of each element in nZVIPs@Ti$_3$C$_2$ nanosheets presented in Table S1.† Also, the surface oxidation of nZVIPs inevitably occurred during the synthesis process due to reactions of nZVIPs with the aqueous solution or air, resulting in the formation of a core–shell morphology as illustrated in Fig. S7 (ESI†). Furthermore, the two lattice fringe spacings of nZVIPs@Ti$_3$C$_2$ nanosheets were about 0.20 nm and 0.31 nm, which were assigned to the (110) crystal plane of zero-valent iron with a diffraction peak at 44.6° and (110) reflection of Ti$_3$C$_2$-based MXene with a diffraction peak at 60.7°, respectively (Fig. 1k).[34,35] Meanwhile, the optimized atomic structures of bi-active centers provided by nZVIPs@Ti$_3$C$_2$-based MXene were theoretically modeled as described in Fig. 1l, on which the adsorption of the PMS molecule had the lowest energy (Fig. S8, ESI†).

Moreover, wide angle X-ray diffraction analysis was conducted to determine whether the Ti$_3$AlC$_2$ particle powder was successfully converted into Ti$_3$C$_2$-based MXene as shown in Fig. 2a, S9 and S10 (ESI†). XRD results clearly showed a shift of the (002) and (004) peaks to lower angles and the weakening of the diffraction peak from the (104) plane at 39.0° (2θ), indicating that the interaction between layers was weakened by HCl and LiF etching.[36,37] FT-IR and Raman results (Fig. 2b and c) revealed that the etching process retained the functional end groups on the surface with abundant C=O bonds and –OH groups on the surface of nZVIPs@Ti$_3$C$_2$ nanosheets. Besides, the nitrogen adsorption–desorption isotherms of nZVIPs, Ti$_3$C$_2$-based MXene and nZVIPs@Ti$_3$C$_2$ nanosheets are shown in Fig. 2d. The observed typical type IV isotherms with type H3 hysteresis loops show that the synthesized catalytic materials exhibited mesoporous structure characteristics.[38] The BJH desorption technology was also employed to establish the corresponding pore size/volume distribution curve (Fig. 2d inset), further demonstrating that the synthetic nZVIPs@Ti$_3$C$_2$ nanosheets were mainly mesoporous (range in 2–50 nm).[39] The specific surface area of pure Ti$_3$C$_2$-based MXene was up to 107.82 m^2 g^{-1}. Importantly, the BET surface area of nZVIPs@Ti$_3$C$_2$ nanosheets (28.25 m^2 g^{-1}) increased by nearly 2-fold compared with that of pure nZVIPs (14.56 m^2 g^{-1}) (Table S2†).

3.2 Interactive relationship between experimental parameters

The response surface method (RSM) is an effective experimental method that allows analysis of the interaction between various factors (*e.g.* pH, and dosage), including screening of the main impact factors, polynomial modeling, and determination of the optimal combination of reactive conditions. Meanwhile, the proposed method was also used to investigate the significance of one parameter and the interaction of these impact factors on ranitidine removal.

3.2.1 Polynomial modeling and variance analysis. The process conditions were optimized according to a Box–Behnken design (BBD) methodology using four factors at three levels, as listed in Table 1. The entire experimental design was
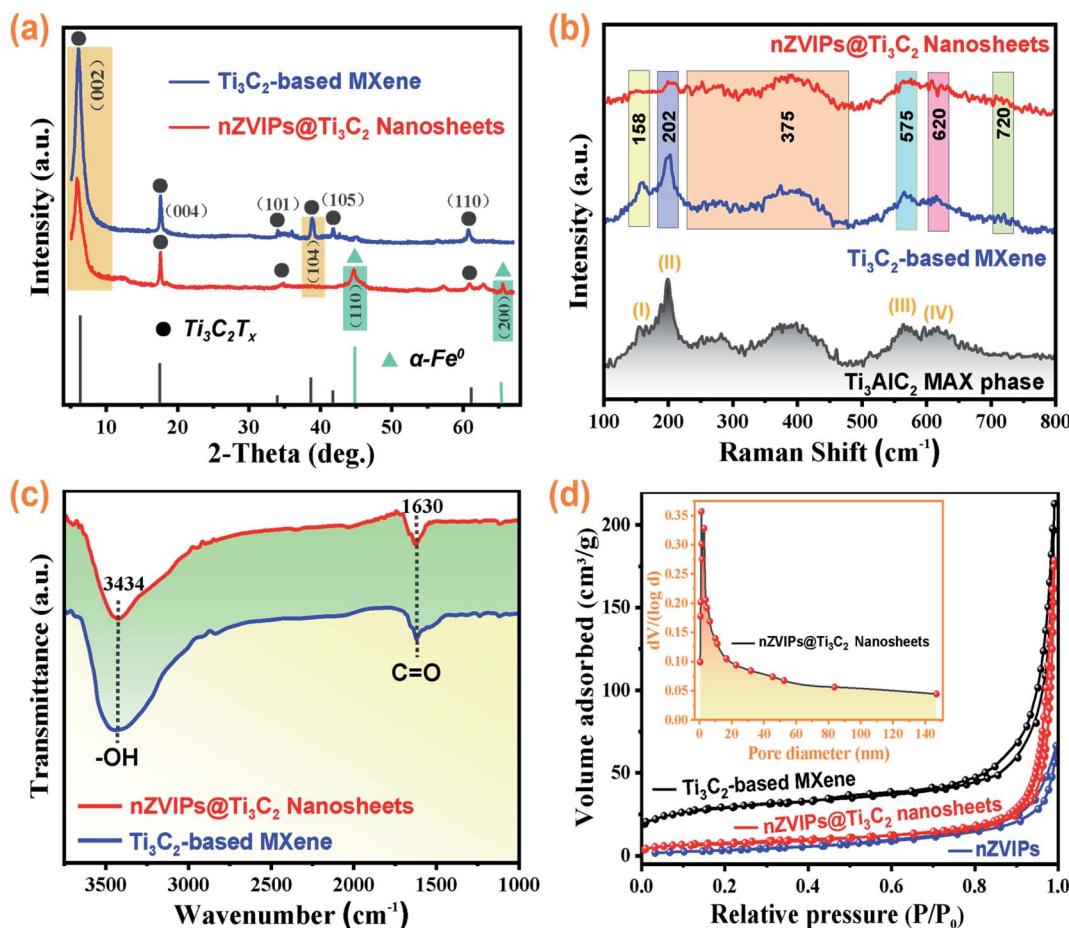
19820 | *J. Mater. Chem. A*, 2021, **9**, 19817–19833

This journal is © The Royal Society of Chemistry 2021

Fig. 2 (a) XRD patterns of Ti_3C_2-based MXene and nZVIPs@Ti_3C_2 nanosheets; (b) Raman spectra of Ti_3AlC_2 pre- and post-etching treatment, and nZVIPs@Ti_3C_2 nanosheets; (c) FTIR spectra of Ti_3C_2-based MXene and nZVIPs@Ti_3C_2 nanosheets; (d) nitrogen adsorption–desorption isotherms for nZVI particles, Ti_3C_2-based MXene and nZVIPs@Ti_3C_2 nanosheets (inset: pore size distribution curve for nZVIPs@Ti_3C_2 nanosheets).

Table 1 Test factor levels and coding system

Variate	Test factors	Levels and coding		
		−1	0	1
X_1	Initial solution pH values	3.5	4.5	6.0
X_2	Dosage of PMS/(mg per 100 mL)	5	10	20
X_3	Dosage of nZVIPs@Ti_3C_2 nanosheets/(mg per 100 mL)	5	7.5	10
X_4	The mass ratio of nZVI : Ti_3C_2	1:2	1:1	2:1

established using Design-Expert 8.0.6 software as illustrated in Table S3,† in which twenty-seven sets of experimental runs were measured and three replicate centers were established to estimate the pure error. Taking the ranitidine removal efficiency as the response value (Y) and fitting the experimental data with polynomial regression analysis,[40] a quadratic polynomial model for the response value with an independent variable (X_i) was obtained, as shown in eqn (3) as follows:

$$\begin{aligned}
Y = {} & -275.53941 + 113.85124X_1 + 6.13678X_2 + 14.28876X_3 \\
& + 24.64529X_4 - 0.37436X_1X_2 + 0.25721X_1X_3 + 0.49375X_1X_4 \\
& + 0.065196X_2X_3 - 0.021541X_2X_4 - 0.29444X_3X_4 \\
& - 12.53077X_1^2 - 0.14397X_2^2 - 1.01691X_3^2 - 8.96577X_4^2 \quad (3)
\end{aligned}$$

These coefficients effectively determined the relationship between their corresponding terms and the surface response.[41] In addition, ANOVA analysis was performed to reliably verify the relevance of the quadratic polynomial model,[42] with the corresponding outcomes for the proposed model shown in Table S4.† Based on the experimental results, the F-value of 181.45 was much higher than 1 and the p-value was below the significance level of 0.05, indicating that this proposed model was suitable for data fitting.[43] The corresponding F-values for initial solution pH (X_1), the PMS dosage (X_2), the nZVIPs@Ti_3C_2 nanosheet dosage (X_3), and the mass ratio of nZVI : Ti_3C_2 (X_4) were 451.74, 489.67, 15.86, and 14.46, respectively, confirming

This journal is © The Royal Society of Chemistry 2021

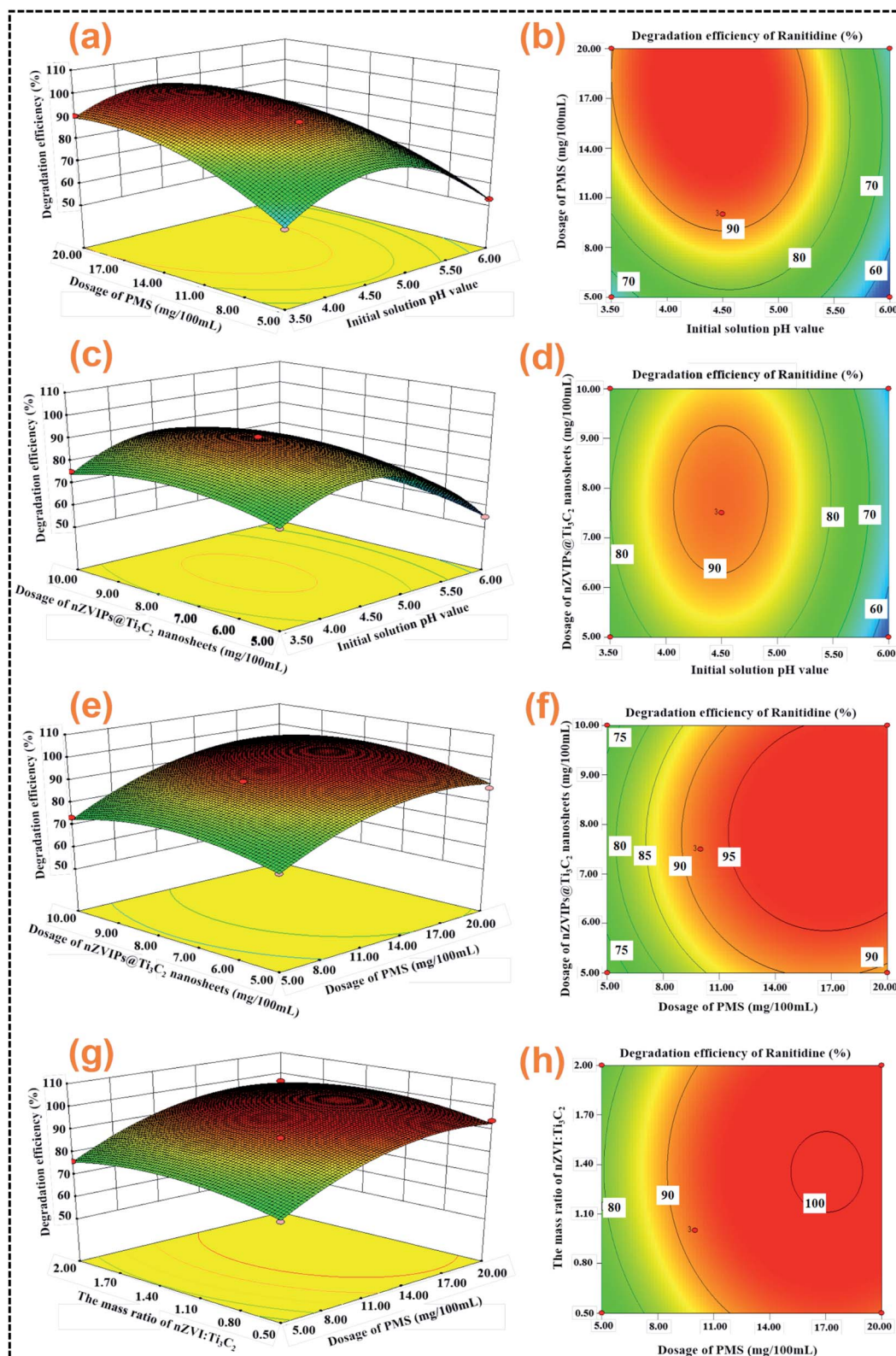*J. Mater. Chem. A*, 2021, **9**, 19817–19833 | **19821**

Fig. 3 Three-dimensional and contour maps of the interaction between different factors for ranitidine degradation efficiency, (a) and (b) initial solution pH value and PMS dosage; (c) and (d) initial solution pH value and dosage of nZVIPs@Ti$_3$C$_2$ nanosheets; (e) and (f) PMS dosage and the dosage of nZVIPs@Ti$_3$C$_2$ nanosheets; (g) and (h) PMS dosage and the mass ratio of nZVI : Ti$_3$C$_2$.

19822 | J. Mater. Chem. A, 2021, 9, 19817–19833

This journal is © The Royal Society of Chemistry 2021

that the initial solution pH and PMS dosage were important factors affecting the ranitidine removal efficiency.

In general, the determination coefficient R^2 and adjusted determination coefficient R_{adj}^2 are indispensable parameters that are universally used to evaluate the reliability and accuracy of polynomial models.[44,45] As shown in Table S4,† the R^2 and R_{adj}^2 values were 0.9953 and 0.9898, respectively, indicating that the regression equation shown in eqn (3) could simulate the actual response surface well. Furthermore, the standardized residual indicated that the data points of standard deviation deviated from both the response value and the measured value were normally distributed. As shown in Fig. S11 (ESI†), these experimental data points were well fitted with the modelled line, indicating that the predicted values were close to the actual values.

3.2.2 Effect of interaction between various factors on the removal of ranitidine. The three-dimensional (3D) response surface plots and two-dimensional (2D) contour plots were used to reflect the interactions between various factors on ranitidine

removal.[46,47] Two distinct shapes could be observed in the 2D contour plots, circle and ellipse, with elliptical contour plots in particular implying that the interactions between variables were significant.[48] The solution pH is an important parameter in iron-based oxidation systems, as it significantly affects the series of reactions, such as the decomposition of oxidants and the generation of radicals. Furthermore, the solution pH also affects the speciation of activated radicals and the distribution of oxidants.[49,50] As shown in Fig. 3a and b, the ranitidine removal efficiency was enhanced with increasing PMS dosages at fixed solution pH values, due to the generation of more active radicals (such as $HO^•$ and $SO_4^{•-}$) in the solution. Although PMS itself has a certain oxidative capacity, it still requires activation to generate $SO_4^{•-}$ and $HO^•$, which are the main oxidants required to achieve degradation of target contaminants, with $SO_4^{•-}$ being prominent under acidic conditions while $HO^•$ is more dominant under basic conditions.[51] However, $HO^•$ has a lower redox potential (1.8 V) under neutral and basic conditions than under acid conditions (2.7 V), and its life span was
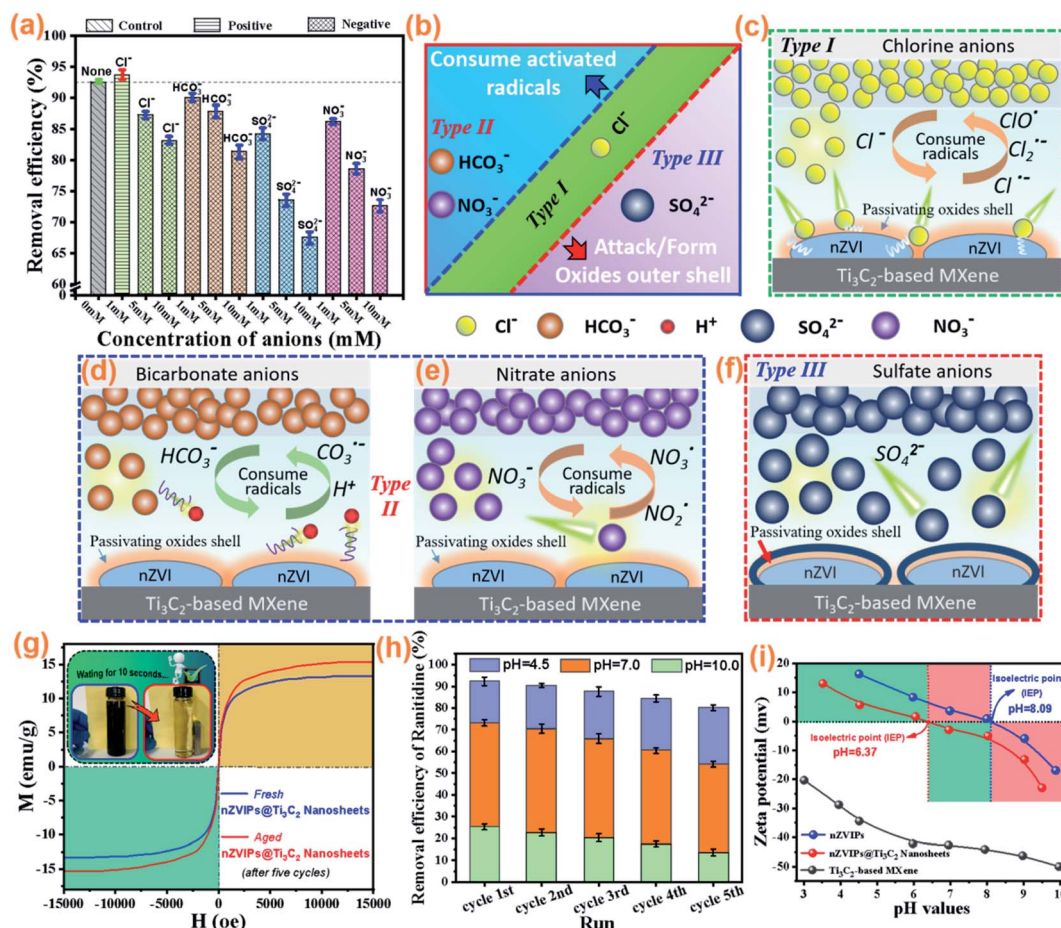

Fig. 4 (a) Effects of common inorganic anions on ranitidine removal in the nZVIPs@Ti$_3$C$_2$ nanosheets/PMS system after 6 min of reaction; (b) the different types of negative effects on ranitidine degradation by common inorganic anions, including (c) chlorine anions (Cl$^-$), (d) bicarbonate anions (HCO$_3^-$), (e) nitrate anions (NO$_3^-$), and (f) sulfate anions (SO$_4^{2-}$), (g) magnetic hysteresis loops of freshly prepared nZVIPs@Ti$_3$C$_2$ nanosheets and nZVIPs@Ti$_3$C$_2$ nanosheets after five cycles of reuse (inset: response of fresh nZVIPs@Ti$_3$C$_2$ nanosheets to an external magnetic field); (h) reuse of nZVIPs@Ti$_3$C$_2$ nanosheets for five consecutive experimental cycles under different solution pH conditions; (i) zeta (ζ)-potential as a function of solution pH (dosage of synthetic materials = 0.5 g L^{-1}). Experimental conditions: [ranitidine]$_0$ = 10 mg L^{-1}, [PMS]$_0$ = 0.1 g L^{-1}, [Cata]$_0$ = 75 mg L^{-1}, nZVI/Ti$_3$C$_2$ mass ratio = 1 : 1, the initial solution pH = 4.5, at room temperature.

shorter than that of $SO_4^{\cdot-}$.[52] Furthermore, with an increase in solution pH, the recombination rate of $SO_4^{\cdot-}$ was much higher than the rate of conversion to $HO^{\cdot}$.[53–55] It has been demonstrated that excessive PMS can also serve as a scavenger for $SO_4^{\cdot-}$ as demonstrated by eqn (4).[18] Since the maximum dosage of PMS was below that limit in the present study, the ranitidine removal efficiency exhibited a trend of continuous increase.
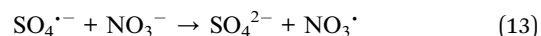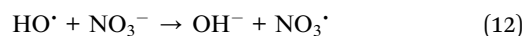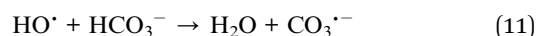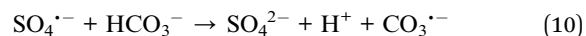
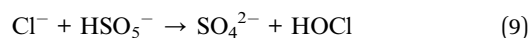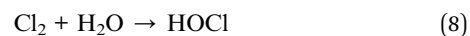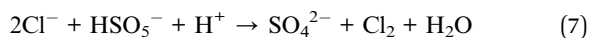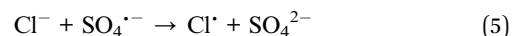$$HSO_5^- + SO_4^{\cdot-} \rightarrow SO_4^{2-} + SO_5^{\cdot-} + H^+ \tag{4}$$
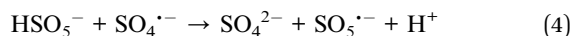
In addition, the ranitidine removal efficiency was enhanced with increased concentrations of nZVIPs@Ti$_3$C$_2$ nanosheets when the dosage was below 0.75 g L^{-1} as depicted in Fig. 3c and d. However, a further increase in the dosage of nZVIPs@Ti$_3$C$_2$ nanosheets resulted in a negative effect on catalytic performance and subsequently a decrease in ranitidine removal. The effect of initial solution pH on ranitidine removal was investigated over a pH range of 3.5–10.0 without buffering (Fig. S12, S13 and Table S5†). Acidic conditions were more favorable for the activation of PMS in this heterogeneous catalytic system, as nZVIPs served as a controllable and slow-releasing source of ferrous ions which could be corroded rapidly, especially under acidic conditions.[56] The core–shell structure not only protects the inner core of nZVIPs from rapid oxidation, but also assists the adsorption of target contaminant molecules due to electrostatic interactions and surface complexation.[57] However, when the initial solution pH values were excessively high, various corrosion products (*e.g.* magnetite, and goethite) accumulate and attach to the surface active sites, interrupting the direct contact between the ZVIP inner core and ranitidine molecules. Fig. 3e–h show that the ranitidine removal efficiency changed significantly under the interaction of nZVIPs@Ti$_3$C$_2$ nanosheets and PMS. PMS was found to have a more significant effect on the removal efficiency of ranitidine, and nZVIPs@Ti$_3$C$_2$ nanosheets, serving as an effective PMS activator, enhanced the generation of active radicals for ranitidine removal. Moreover, the interactions between other various factors on ranitidine removal were discussed in detail as shown in Fig. S14.†

3.3 Effects of dissolved anions on ranitidine degradation in nZVIPs@Ti$_3$C$_2$ nanosheets/PMS system

Inorganic anions are commonly present in water bodies, which may affect the performance of pollutant removal by catalysts, including buffering the solution pH, capturing activated radicals and mitigating the effect of electrostatic bonds between reactants.[58,59] As such, common inorganic anions such as Cl$^-$, HCO$_3^-$, SO$_4^{2-}$ and NO$_3^-$ were added to the bulk solution in the form of sodium salts to investigate their interference to ranitidine degradation by the nZVIPs@Ti$_3$C$_2$ nanosheets/PMS system as shown in Fig. 4a–f.

Fig. 4a depicts the effects of the various inorganic anions with the concentrations of 1, 5 and 10 mM on ranitidine removal efficiency in the nZVIPs@Ti$_3$C$_2$ nanosheets/PMS system. The ranitidine removal efficiency slightly increased from 92.62% to 93.72% after the addition of 1 mM Cl$^-$, while

gradually decreasing to 87.27% and 83.21% in 6 min as the dosage of Cl$^-$ was increased to 5 and 10 mM, respectively. This is possibly because Cl$^-$ penetrates the passivating oxide layer by diffusion, forming complexes with the zero-valent iron inner core and greatly accelerating the corrosion of nZVIPs (Fig. 4c).[60] Additionally, excessive Cl$^-$ can also consume activated radicals and HSO$_5^-$, generating less reactive chloride radical anions (Cl$^{\cdot}$, Cl$_2^{\cdot-}$ and ClO$^{\cdot}$) and hypochlorous species (eqn (5)–(9)). The redox potentials of Cl$^{\cdot}$ and Cl$_2^{\cdot-}$ are 2.4 V and 2.1 V, respectively, both of which are lower than that of SO$_4^{\cdot-}$ (2.5–3.1 V).[61–63] When HCO$_3^-$ was added to the bulk solution, significant inhibition was observed that the ranitidine removal efficiency decreased from 92.62% to 90.06%, 87.83% and 81.31% in the presence of 1, 5 and 10 mM HCO$_3^-$, respectively. The dissolved HCO$_3^-$ could serve as a scavenger, consuming both SO$_4^{\cdot-}$ and HO$^{\cdot}$ to yield less active radical species (eqn (10) and (11)) (Fig. 4d).[55] Furthermore, HCO$_3^-$ anions are basic agents capable of producing a buffering effect on the solution, resulting in an increase in the solution pH that was unfavorable for ranitidine removal.[64]

$$Cl^- + SO_4^{\cdot-} \rightarrow Cl^{\cdot} + SO_4^{2-} \tag{5}$$

$$Cl^- + Cl^{\cdot} \rightarrow Cl_2^{\cdot-} \tag{6}$$

$$2Cl^- + HSO_5^- + H^+ \rightarrow SO_4^{2-} + Cl_2 + H_2O \tag{7}$$

$$Cl_2 + H_2O \rightarrow HOCl \tag{8}$$

$$Cl^- + HSO_5^- \rightarrow SO_4^{2-} + HOCl \tag{9}$$

$$SO_4^{\cdot-} + HCO_3^- \rightarrow SO_4^{2-} + H^+ + CO_3^{\cdot-} \tag{10}$$

$$HO^{\cdot} + HCO_3^- \rightarrow H_2O + CO_3^{\cdot-} \tag{11}$$

$$HO^{\cdot} + NO_3^- \rightarrow OH^- + NO_3^{\cdot} \tag{12}$$

$$SO_4^{\cdot-} + NO_3^- \rightarrow SO_4^{2-} + NO_3^{\cdot} \tag{13}$$

$$H_2O + e_{aq}^- + NO_3^- \rightarrow 2OH^- + NO_2^{\cdot} \tag{14}$$

In addition, both NO$_3^-$ and SO$_4^{2-}$ exhibited highly negative effects on ranitidine degradation, with SO$_4^{2-}$ anions exerting the most significant inhibition effect. The significant inhibitory effect of NO$_3^-$ on ranitidine removal was due to the reactions of NO$_3^-$ anions with dissolved electrons and activated radicals (SO$_4^{\cdot-}$ and HO$^{\cdot}$) with the conversion to less active species (Fig. 4e), such as NO$_3^{\cdot}$ and NO$_2^{\cdot}$ (eqn (12)–(14)).[55] When SO$_4^{2-}$ was present in the bulk solution with the concentrations of 1, 5 and 10 mM, the ranitidine removal efficiency in 6 min decreased to 84.26%, 73.55% and 67.45%, respectively. This could be attributed to the formation of inner-sphere complexes on the nZVIP surface, blocking the electron transport pathway (Fig. 4f).[65]

3.4 Reusability and stability of nZVIPs@Ti$_3$C$_2$ nanosheets

The magnetic properties of nZVIPs@Ti$_3$C$_2$ nanosheets before and after the ranitidine degradation reaction were measured

19824 | *J. Mater. Chem. A*, 2021, **9**, 19817–19833

This journal is © The Royal Society of Chemistry 2021

with the corresponding magnetization hysteresis loops shown in Fig. 4g. The saturation magnetization value of nZVIPs@Ti$_3$C$_2$ nanosheets before the reaction was 13.2 emu g^{-1}, while that increased to 15.3 emu g^{-1} after five consecutive cycles of use. These results indicated that strong magnetic iron oxides were formed on the nZVIP surface. Additionally, nZVIPs@Ti$_3$C$_2$ nanosheets could be conveniently separated from the reaction mixture for reuse by applying an external magnetic field, which is an important physical property for nanocomposite catalytic materials.

Considering that acidic conditions are conducive to etching of the passivated layer on the surface of nZVIPs, it is important to conduct cyclic experiments of nZVIPs@Ti$_3$C$_2$ nanosheets under different solution pH conditions. As shown in Fig. 4h, although the removal efficiency slightly decreased with each experimental cycle, nZVIPs@Ti$_3$C$_2$ nanosheets retained high catalytic activity especially under acidic conditions. To avoid further oxidation of nZVIPs in composition before the next experimental cycle, nitrogen protection was conducted with the detailed method of nZVIPs@Ti$_3$C$_2$ recovery shown in Fig. S15.† Additionally, the isoelectric point (pH$_{pzc}$) of nZVIPs@Ti$_3$C$_2$ nanosheets was about 6.37 as shown in Fig. 4i, suggesting that the surface of the composite exhibited a positive charge when the solution pH was below 6.37. Therefore, when the initial solution pH was adjusted to 3.5–6.0, the electrical interaction between HSO$_5$$^-$ and nZVIPs@Ti$_3$C$_2$ nanosheets favored their contact, accelerating the activation of PMS. When the initial solution pH was 4.5, the ranitidine removal efficiency reached 92.31%, 90.46%, 87.68%, 84.45%, and 80.29% in five consecutive cycles, respectively. As the initial solution pH further increased to neutral and alkaline levels, the catalytic activity of nZVIPs@Ti$_3$C$_2$ nanosheets was limited to varying degrees, while the ranitidine removal efficiency was not significantly reduced, indicating that nZVIPs@Ti$_3$C$_2$ nanosheets exhibited good stability in aqueous solution. Furthermore, the leaching behavior of the Fe element at the acidic pH of 4.5 during the
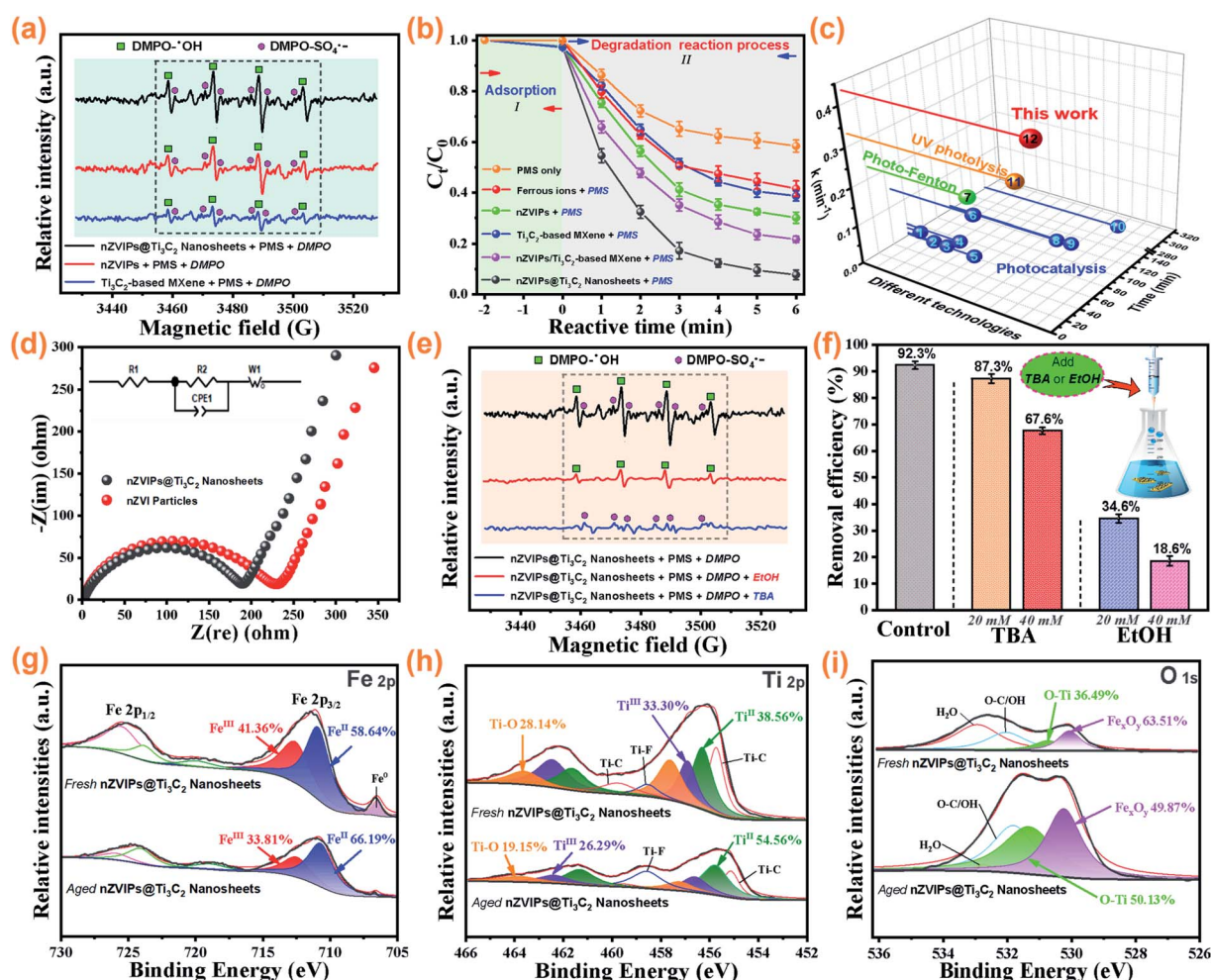

Fig. 5 (a) EPR spectra of different reaction systems using DMPO as the trapping agent at 3 min ([DMPO]$_0$ = 0.1 M, V_{DMPO} = 50 μL, V_{sample} = 2 mL); (b) the removal of ranitidine in different reaction systems; (c) comparison of ranitidine removal efficiency over different technologies; (d) AC impedance plots for nZVIPs and nZVIPs/Ti$_3$C$_2$ nanosheets (inset: the equivalent circuit); (e) EPR spectra under various conditions at 3 min ([EtOH]$_0$ = 20 mM, [TBA]$_0$ = 20 mM); (f) the effects of different quenching agent concentrations on ranitidine removal; XPS spectra of nZVIPs@Ti$_3$C$_2$ nanosheets before and after reaction; narrow region scans of (g) Fe$_{2p}$ and (h) Ti$_{2p}$; (i) O$_{1s}$. Experimental conditions: [ranitidine]$_0$ = 10 mg L^{-1}, [PMS]$_0$ = 0.1 g L^{-1}, [Cata]$_0$ = 75 mg L^{-1}, nZVI/Ti$_3$C$_2$ mass ratio = 1 : 1, the initial solution pH = 4.5, at room temperature.

This journal is © The Royal Society of Chemistry 2021

J. Mater. Chem. A, 2021, **9**, 19817–19833 | **19825**

catalytic process in Fig. S16† shows that the maximum concentrations of total iron and ferrous ions in solution are 2.65 mg L^{-1} and 0.41 mg L^{-1}, respectively.

3.5 Identification of radical species generated in the nZVIPs@Ti$_3$C$_2$ nanosheets/PMS system
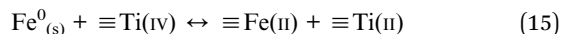
To clarify the mechanism of PMS activation, EPR experiments employing the spin-trapping agent DMPO were performed to identify the free radicals involved in the nZVIPs@Ti$_3$C$_2$ nanosheets/PMS reaction system. Three groups of EPR signals with different response intensities were observed when nZVIPs, Ti$_3$C$_2$-based MXene and nZVIPs@Ti$_3$C$_2$ nanosheets were present in the bulk solution with the addition of PMS, as shown in Fig. 5a. These signal peaks were assigned to the hyperfine splitting of DMPOX adducts, which may be attributed to highly reactive oxidizing species (SO$_4^{\bullet-}$ and HO$^\bullet$) generated during PMS activation.[66,67] Furthermore, the relative intensities of both DMPO–SO$_4^{\bullet-}$ and DMPO–$^\bullet$OH adducts were higher in the nZVIPs@Ti$_3$C$_2$ nanosheets/PMS system compared to those of both the nZVI/PMS system and the Ti$_3$C$_2$-based MXene/PMS system, indicating that nZVIPs@Ti$_3$C$_2$ nanosheets activated PMS and enhanced the production of SO$_4^{\bullet-}$ and HO$^\bullet$. Interestingly, both nZVIPs and Ti$_3$C$_2$-based MXene in nZVIPs@Ti$_3$C$_2$ nanosheets exhibited catalytic activity for PMS activation, further confirming that this composite provided bi-active surface sites for the formation of SO$_4^{\bullet-}$ and HO$^\bullet$. In order to verify these findings, the degradation of ranitidine using different catalysts was compared, as shown in Fig. 5b. A significantly higher removal efficiency was achieved in 6 min when any solid catalyst was added into the bulk solution compared to the case with ferrous ions, indicating that surface active sites provided by solid catalysts played a major role in the rapid decomposition of ranitidine. Both nZVIPs and Ti$_3$C$_2$-based MXene could activate PMS to generate SO$_4^{\bullet-}$ and HO$^\bullet$ for the degradation of ranitidine molecules, and the corresponding removal efficiency by nZVIPs was higher than that by Ti$_3$C$_2$-based MXene. However, it was difficult to achieve a high ranitidine removal efficiency when merely utilizing a mixture of nZVIPs, Ti$_3$C$_2$-based MXene and PMS. This result indicates that the synergistic interaction between nZVIPs and Ti$_3$C$_2$-based MXene was more conducive to the catalytic degradation of ranitidine in the PMS-induced heterogeneous oxidation system. It is worth mentioning that the kinetic rate constant for the degradation of ranitidine by the nZVIPs@Ti$_3$C$_2$ nanosheets/ PMS system was much larger (1.3–136.9-fold) than the reported values as shown in Fig. 5c and Table S6,† indicating the remarkable efficiency of this nZVIPs@Ti$_3$C$_2$ nanosheets/PMS heterogeneous Fenton-like catalysis.

Furthermore, electrochemical impedance spectroscopy (EIS) measurements were carried out to investigate the conductivity of nZVIPs and nZVIPs@Ti$_3$C$_2$ nanosheets. As shown in Fig. 5d, the Nyquist plots of the synthesized nZVIPs and nZVIPs@Ti$_3$C$_2$ nanosheet electrodes consisted of semicircles in the high/medium frequency ranges and straight lines in low frequency ranges, corresponding to the charge transfer resistance (R_{ct}) and Warburg impedance associated with Li-ion diffusion in the electrode.[68,69] The

semicircle diameter of the plot for the nZVIPs@Ti$_3$C$_2$ nanosheet electrode was significantly smaller than that for the nZVIPs electrode, mainly due to the enhanced electroconductibility of nZVIPs@Ti$_3$C$_2$ nanosheets. The smaller R_{ct} of nZVIPs@Ti$_3$C$_2$ nanosheets (187.3 Ω) demonstrated that this composite exhibited a greater charge transfer capability compared to nZVIPs (227.0 Ω). The results of these experiments indicated that PMS activation occurred mainly at the surface active sites of nZVIPs@Ti$_3$C$_2$ nanosheets, with SO$_4^{\bullet-}$ and HO$^\bullet$ being the main active oxidation species for the degradation of ranitidine, but these results did not determine whether SO$_4^{\bullet-}$ or HO$^\bullet$ was the most dominant species. In generally, ethanol (EtOH) and *tert*-butyl alcohol (TBA) are commonly used as scavengers for quenching free radicals (k(SO$_4^{\bullet-}$, EtOH) = 1.6–7.7 × 10^7 M^{-1} s^{-1}, k(HO$^\bullet$, EtOH) = 1.2–2.8 × 10^9 M^{-1} s^{-1} and k(HO$^\bullet$, TBA) = 3.8–7.6 × 10^8 M^{-1} s^{-1}), with EtOH considered as a scavenger of both SO$_4^{\bullet-}$ and HO$^\bullet$ while TBA scavenges HO$^\bullet$ only.[70–72] When 20 mM TBA was added into the aqueous solution, the DMPO–SO$_4^{\bullet-}$ signal detected in the nZVIPs@Ti$_3$C$_2$ nanosheets/PMS system was consistent with the selective scavenging of HO$^\bullet$ in the bulk solution by TBA, as illustrated in Fig. 5e. However, the weak EPR signal of DMPO–HO$^\bullet$ could still be observed with the addition of 20 mM of EtOH, which might be due to insufficient use of the scavenger, resulting in a small fraction of free radicals not being quenched completely. Fig. 5f shows that the removal of ranitidine was inhibited significantly when different concentrations of EtOH and TBA were added into the solution. In particular, the corresponding ranitidine removal efficiency was reduced from 34.6% to 18.6% when the concentration of EtOH increased from 20 mM to 40 mM. Comparison of the inhibition effects of EtOH and TBA on ranitidine removal shows that SO$_4^{\bullet-}$ and HO$^\bullet$ derived from PMS activation are generated in the nZVIPs@Ti$_3$C$_2$ nanosheets/PMS system, with SO$_4^{\bullet-}$ serving as the dominant oxidative species for ranitidine degradation.

3.6 Verification of surface element components of bi-active centers provided by nZVI@Ti$_3$C$_2$ nanosheets

The chemical states of Fe (2p), Ti (2p) and O (1s) elements on the surface of nZVIPs@Ti$_3$C$_2$ nanosheets were analyzed by XPS measurements before and after the ranitidine degradation reaction, as shown in Fig. 5g–i. The satellite peaks referring to Fe (2p$_{1/2}$) and Fe (2p$_{3/2}$) could be observed by spin–orbit doublets with binding energies of 724.6 and 711.4 eV, respectively (Fig. 5g). Particularly for the Fe (2p$_{3/2}$) peak, two components centering at binding energies of 710.7 and 712.5 eV in both fresh and aged nZVIPs@Ti$_3$C$_2$ nanosheets were indicative of the existence of iron-based species derived from Fe(II) and Fe(III).[34] The relative ratios of Fe(II) and Fe(III) peak areas in the fresh sample were 58.64% and 41.36%, respectively, while the equivalent ratios in the aged sample were 66.19% and 33.81%. It is of note that both Fe(II) and Fe(III) are involved in PMS activation, with an electron transfer cycle formed between Fe(II) and Fe(III). Moreover, the peak intensity of nZVI in aged nZVIPs@Ti$_3$C$_2$ nanosheets was significantly decreased, due to nZVI particles serving as an electron donor and the increasing thickness of the oxide layer on the particle surface.

19826 | *J. Mater. Chem. A*, 2021, **9**, 19817–19833

This journal is © The Royal Society of Chemistry 2021

$$Fe^0_{(s)} + \equiv Ti(IV) \leftrightarrow \equiv Fe(II) + \equiv Ti(II) \quad (15)$$

The XPS spectra for Ti (2p) clearly show that there were mainly three valence forms of Ti in Ti_3C_2-based MXene components (Fig. 5h). An increase in the proportion of Ti(II) from 38.56% (fresh sample) to 54.56% (aged sample) suggested that Ti_3C_2-based MXene continuously accepted electrons from nZVIPs (eqn (15)), further indicating that nZVIPs and Ti_3C_2-based MXene interacted through charge transfer between

transition metals with the formation of surface $\equiv Fe(II)$ and the release of ferrous ions into aqueous solution to stimulate the heterogeneous and homogeneous Fenton-like reactions. Although these reactions were conducive to the rapid removal of ranitidine, catalysts were inevitably consumed. After the reaction with PMS, distinct Ti–O and Fe_xO_y peaks were detected in the aged sample, as shown in Fig. 5i, which could result from the consumption of the bi-active sites on the surface of nZVIPs@Ti_3C_2 nanosheets. The O (1s) spectrum results are in
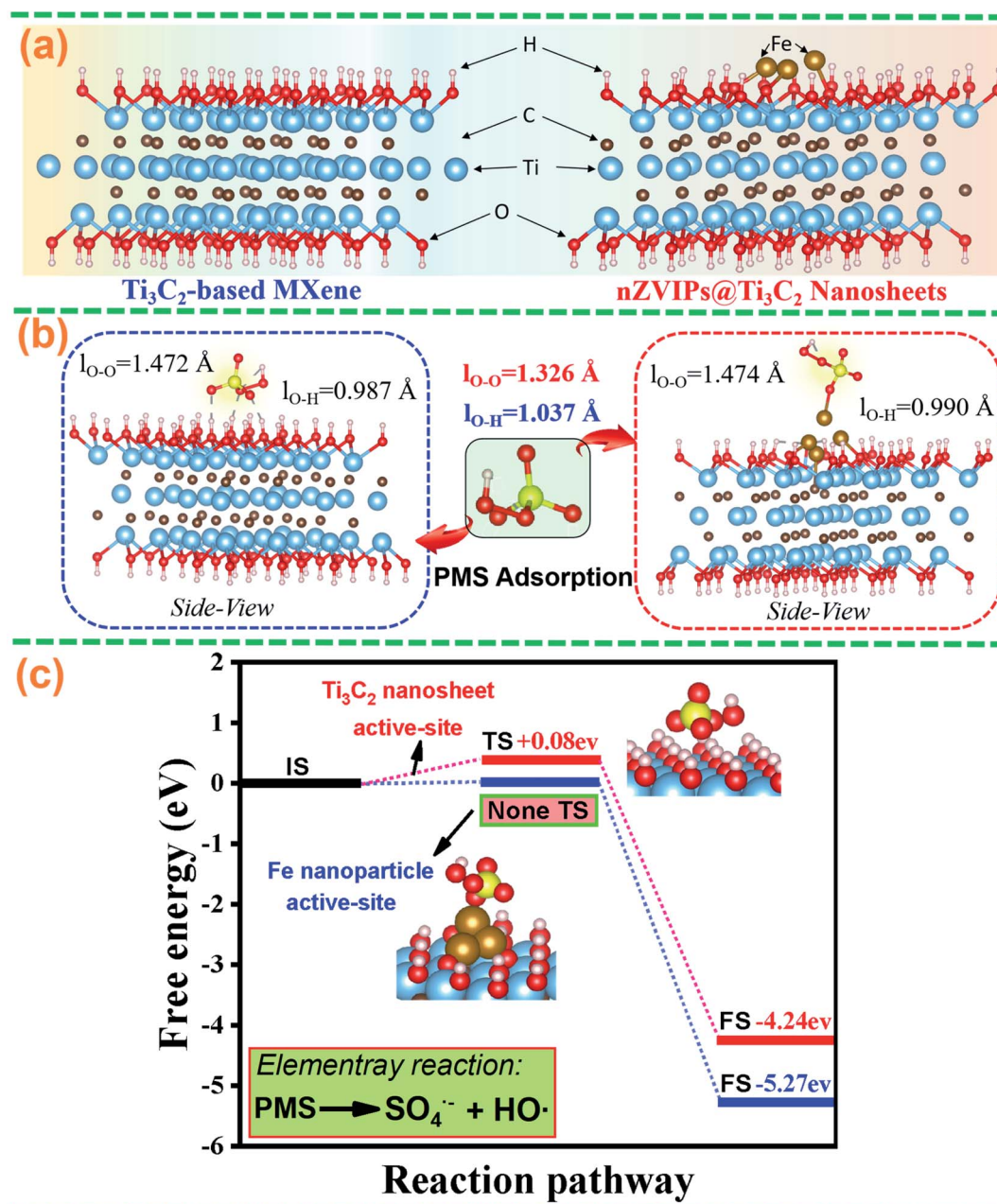

Fig. 6 DFT calculations of PMS activation by nZVIPs@Ti_3C_2 nanosheets and Ti_3C_2-based MXene, (a) atomic structures of Ti_3C_2-based MXene and nZVIPs@Ti_3C_2 nanosheets; (b) calculated l_{O-O} and l_{O-H} bond lengths, and free energy evolution of PMS molecules on the surface of Ti_3C_2-based MXene and nZVIPs@Ti_3C_2 nanosheets, respectively; (c) reaction pathway of the activation of PMS on the surface of nZVIPs@Ti_3C_2 nanosheets, where IS, TS and FS represent the initial structure, transition structure and final structure, respectively; blue, brown, gold, yellow, red, and white balls represent Ti, C, Fe, S, O, and H atoms, respectively.

This journal is © The Royal Society of Chemistry 2021

J. Mater. Chem. A, 2021, 9, 19817–19833 | 19827

line with the evidence that the oxidation in the PMS-induced heterogeneous Fenton-like reaction favored the formation of iron-based oxides.

3.7 DFT calculations of PMS activation by nZVIPs@Ti$_3$C$_2$ nanosheets
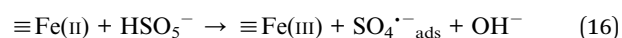
Density functional theory (DFT) calculations were performed to investigate the adsorption and activation behavior of PMS molecules on the surface of nZVIPs@Ti$_3$C$_2$ nanosheets and to understand the roles of bi-active surface centers in promoting PMS activation. As shown in Fig. 6a, the optimized structures of Ti$_3$C$_2$-based MXene and nZVIPs@Ti$_3$C$_2$ nanosheets were theoretically modeled. When PMS molecules were adsorbed on the surface of Ti$_3$C$_2$-based MXene and nZVIPs@Ti$_3$C$_2$ nanosheets, the possible adsorption configurations with the lowest energy are illustrated in Fig. 6b, and the corresponding adsorption energies and bond length (l_{O-O} and l_{O-H} in the PMS molecule structure) are also listed in Table S7.† The theoretical l_{O-O} bond length of the free PMS molecule was 1.326 Å,[73] while the l_{O-O} bond was remarkably stretched when PMS molecules were adsorbed on the Fe nanoparticle (1.474 Å) and Ti$_3$C$_2$ nanosheet (1.472 Å) surface active-sites, indicating that these adsorbed PMS molecules tend to decompose. In addition, PMS molecules can be easily adsorbed on the Ti$_3$C$_2$ nanosheet active-site (-5.43 eV) and Fe nanoparticle active-site (-4.84 eV). The more favorable adsorption of PMS molecules on the Ti$_3$C$_2$ nanosheet active-site was due to the surface functional groups (–OH) of Ti$_3$C$_2$-based MXene. As such, nZVIPs@Ti$_3$C$_2$ nanosheets provided bi-active surface centers that could stimulate PMS activation. The reaction energies required for the Fe nanoparticle active-site and Ti$_3$C$_2$ nanosheet active-site to stimulate PMS activation were calculated as shown in Fig. 6c. The reaction energy barrier (E_b) corresponding to the Ti$_3$C$_2$ nanosheet active-site was calculated to be 0.08 eV, much lower than the critical value (0.9 eV) that determined whether a chemical reaction could proceed at room temperature.[74] Besides, the strong interaction between positively charged Fe nanoparticle active-sites and negatively charged PMS molecules (HSO$_5^-$) resulted in the spontaneous dissociation of adsorbed PMS molecules without an energy barrier followed by the formation of SO$_4^{\bullet-}$ and HO$^\bullet$. Additionally, the PMS activation process that occurred on the bi-active surface sites of nZVIPs@Ti$_3$C$_2$ nanosheets and the subsequent PMS dissociation are demonstrated in Fig. S17,† which were thermodynamically favorable. These results further confirm that both the Fe nanoparticle active-site and Ti$_3$C$_2$ nanosheet surface active-site of nZVIPs@Ti$_3$C$_2$ nanosheets enabled the activation of PMS molecules with the yield of highly active radicals for pollutant removal.

3.8 Mechanism of ranitidine degradation in nZVIPs@Ti$_3$C$_2$ nanosheets/PMS system

According to the experimental results discussed, the combination of nZVIPs@Ti$_3$C$_2$ nanosheets and PMS contributed to rapid and efficient removal of ranitidine from aqueous solution. In this heterogeneous Fenton-like oxidation system, PMS was the main source of active oxidation species for ranitidine

degradation, with nZVIPs@Ti$_3$C$_2$ nanosheets providing a large number of active sites that can participate in PMS activation. These active sites replace the dissolved transition metal ions as the catalytic oxidation reaction center, activating PMS to generate highly active free radicals to continuously attack ranitidine molecules until mineralization. EPR results indicated that SO$_4^{\bullet-}$ and HO$^\bullet$ were the main products after PMS activation, with radical quenching experiments further confirming that SO$_4^{\bullet-}$ was the most important active oxidation species for ranitidine removal.

3.8.1 Mechanism of PMS activation by nZVIPs@Ti$_3$C$_2$ nanosheets. Serving as a charge donor and electron-rich center, nZVIPs exhibit excellent reactivity in aqueous solution, generating Fenton reagents involved in ranitidine degradation through rapid charge transfer processes. However, due to the magnetic force between these nanoscale particles, they contact and easily agglomerate into a cluster of particles with a smaller specific surface area. Based on these considerations, the selection of Ti$_3$C$_2$-based MXene as the supporting carrier overcame the problem of nZVIP agglomeration. Therefore, compared with pristine nZVIPs, the specific surface area of nZVIPs@Ti$_3$C$_2$ nanosheets was increased by nearly two-fold (Table S1†), which is an important factor in the enhancement of catalytic performance. Moreover, as discussed in Section 3.7, nZVIPs@Ti$_3$C$_2$ nanosheets provide bi-active surface centers for PMS molecule activation, allowing Ti$_3$C$_2$-based MXene in components to not only be used as a substrate but also to contribute to the highly catalytic effect. This conclusion is consistent with the findings of previous literature.[31] PMS exhibits two different pK_a values, p$K_{a1} < 0$ and p$K_{a2} = 9.4$,[53,75] and as shown in Fig. S18,† HSO$_5^-$ is the dominant species of PMS in the pH range from 3.5 to 9.0, while PMS mainly exists as SO$_5^{2-}$ when solution pH increases to above 9.4. Furthermore, due to the activation of nZVIPs@Ti$_3$C$_2$ nanosheets, the peroxide bond (l_{O-O}) in the HSO$_5^-$ molecule structure was broken to generate highly oxidizing sulfate radicals (SO$_4^{\bullet-}$). On the basis of the above analysis, several possible PMS activation mechanisms have been proposed according to the location of the reactive sites in this composite and the different types of radicals generated by activation, as illustrated in Fig. 7a. Surface active sites composed of low-valence transition metal elements were the most important factors for PMS activation. For nZVIPs@Ti$_3$C$_2$ nanosheets, there were two types of surface-bound active sites that could stimulate PMS activation to yield sulfate radicals (SO$_4^{\bullet-}$), $\equiv$Fe(II) generated by the rapid charge transfer of nZVI and $\equiv$Ti(III) in the Ti$_3$C$_2$-based MXene lattice (eqn (16) and (17)). Meanwhile, $\equiv$Fe(II) can be converted to $\equiv$Fe(III), which subsequently reacts with HSO$_5^-$ to produce SO$_5^{\bullet-}$ with the regeneration of $\equiv$Fe(II) (eqn (18)).[76] These rapid reaction processes lead to the enrichment of a large number of SO$_4^{\bullet-}{}_{ads}$ on the solid catalyst surface, some of which were directly involved in the decomposition of ranitidine molecules, while the remaining SO$_4^{\bullet-}{}_{ads}$ are further converted to hydroxyl radicals (HO$^\bullet{}_{ads}$) through H$_2$O/OH$^-$ oxidation (eqn (19) and (20)).

$$\equiv Fe(II) + HSO_5^- \rightarrow \ \equiv Fe(III) + SO_4^{\bullet-}{}_{ads} + OH^- \qquad (16)$$

Fig. 7 (a) Schematic illustration of the ranitidine degradation mechanism by nZVIPs@Ti$_3$C$_2$ nanosheets with the activation of PMS (transition metal elements with "≡" indicating adsorption on the solid catalyst surface); (b) possible charge transfer pathways in the nZVIPs@Ti$_3$C$_2$ nanosheets/PMS system.

$$\equiv\!Ti(III) + HSO_5^- \rightarrow \ \equiv\!Ti(IV) + SO_4^{\bullet-}{}_{ads} + OH^- \qquad (17)$$

$$\equiv\!Fe(III) + HSO_5^- \rightarrow \ \equiv\!Fe(II) + SO_5^{\bullet-}{}_{ads} + H^+ \qquad (18)$$

$$SO_4^{\bullet-}{}_{ads} + H_2O \rightarrow SO_4^{2-} + HO^{\bullet}{}_{ads} + H^+ \qquad (19)$$

$$SO_4^{\bullet-}{}_{ads} + OH^- \rightarrow SO_4^{2-} + HO^{\bullet}{}_{ads} \qquad (20)$$

$$Fe(II) + HSO_5^- \rightarrow Fe(III) + SO_4^{\bullet-}{}_{free} + OH^- \qquad (21)$$

$$Fe(III) + HSO_5^- \rightarrow Fe(II) + SO_5^{\bullet-}{}_{free} + H^+ \qquad (22)$$
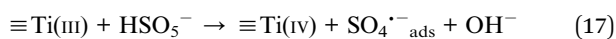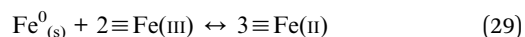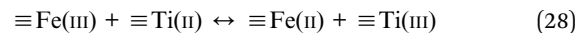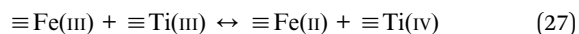
$$SO_4^{\bullet-}{}_{free} + H_2O \rightarrow SO_4^{2-} + HO^{\bullet}{}_{free} + H^+ \qquad (23)$$

$$SO_4^{\bullet-}{}_{free} + OH^- \rightarrow SO_4^{2-} + HO^{\bullet}{}_{free} \qquad (24)$$

$$HO^{\bullet}{}_{ads}/HO^{\bullet}{}_{free} + \text{ranitidine} \rightarrow \text{degraded products} \qquad (25)$$

$$SO_4^{\bullet-}{}_{ads}/SO_4^{\bullet-}{}_{free} + \text{ranitidine} \rightarrow \text{degraded products} \qquad (26)$$

Under acidic conditions, excess hydrogen ions in aqueous solution directly attack the core–shell structure of nZVIPs. This process begins with etching and dissolving the passivated layer on the surface of nZVIPs, with these hydrogen ions reacting with the inner core to release ferrous ions through redox reactions. And then, ferrous ions resulting from the dissolution of nZVIPs diffuse into the bulk solution and induce a series of homogeneous catalytic reactions, activating a small portion of free PMS molecules and generating active radicals including $SO_4^{\bullet-}{}_{free}$ and $HO^{\bullet}{}_{free}$ through a chain reaction (eqn (21)–(24)). Finally, under the combined action of homogeneous and heterogeneous catalysis, ranitidine molecules were degraded mainly by $SO_4^{\bullet-}{}_{ads}/SO_4^{\bullet-}{}_{free}$ and $HO^{\bullet}{}_{ads}/HO^{\bullet}{}_{free}$, existing either in a surface-bound form on nZVIPs@Ti$_3$C$_2$ nanosheets, or free in the bulk solution (eqn (25) and (26)).

3.8.2 Insight into the mode of multiple valence cycles between Fe and Ti elements. In general, the Fe(II)/Fe(III) cycle of most iron-based solid catalysts in heterogeneous Fenton reactions is inferior to that of traditional homogeneous Fenton

reagents, with this performance defect directly affecting the service life of catalytic materials.[26] The Ti element in the molecular structure of Ti$_3$C$_2$-based MXene (valence states of +2, +3 and +4) belonged to a metastable state and due to the standard redox potential of Fe^{3+}/Fe^{2+} being 0.77 V, while that of Ti^{4+}/Ti^{3+} was 0.19 V, the transfer of electrons from ≡Ti(III) to ≡Fe(III) was thermodynamically favored (eqn (27)). Compared with trivalent Ti, divalent Ti exhibits a stronger reduction capacity, achieving Fe(II)/Fe(III) cycling through charge transfer (eqn (28)). The above reaction processes provided the main route for providing ≡Fe(II) and ≡Ti(III) to activate PMS, as well as the core reactions that can achieve recyclable catalysis oxidation.

$$\equiv\!Fe(III) + \ \equiv\!Ti(III) \leftrightarrow \ \equiv\!Fe(II) + \ \equiv\!Ti(IV) \qquad (27)$$

$$\equiv\!Fe(III) + \ \equiv\!Ti(II) \leftrightarrow \ \equiv\!Fe(II) + \ \equiv\!Ti(III) \qquad (28)$$

$$Fe^0{}_{(s)} + 2\!\equiv\!Fe(III) \leftrightarrow 3\!\equiv\!Fe(II) \qquad (29)$$

As discussed, the zero-valent iron inner core with a standard redox potential of -0.44 V can be used as an electron donor to reduce ≡Fe(III) to ≡Fe(II). However, due to the short migration distance of electrons in aquatic media, only a portion of ≡Fe(III) that surrounds the inner core of nZVIPs can receive electrons.[20] The results of electrochemical experiments (Fig. 5d) showed that Ti$_3$C$_2$-based MXene with the excellent electrical conductivity provides stable electron transport channels, which greatly improves the charge transport efficiency between nZVIPs (eqn (29)). It can clearly be seen from Fig. 7b that the synergistic action of multi-valence state cycles was the key to achieving stable catalytic oxidation of ranitidine in the nZVIPs@Ti$_3$C$_2$ nanosheets/PMS heterogeneous reaction system, which was also consistent with the ranitidine removal efficiency dynamics observed in cyclic experiments.

4. Conclusions

In this study, novel magnetic Ti$_3$C$_2$-based MXene nanosheets with nZVIPs uniformly immobilized on the surface in the form of a single-layer covering, served as a solid catalyst for the rapid

This journal is © The Royal Society of Chemistry 2021

J. Mater. Chem. A, 2021, **9**, 19817–19833 | **19829**

removal of ranitidine from aqueous solution. The response surface method (RSM) was used to determine the optimal combination of reaction conditions, among which the initial solution pH and the PMS dosage were the main factors affecting the whole heterogeneous oxidation process. This nZVIPs@Ti$_3$C$_2$ nanosheets/PMS heterogeneous reaction system exhibited a strong resistance to inorganic anion interference and retained excellent reusability and a high level of catalytic activity after five cycles of reuse. This was mainly ascribed to the presence of two types of surface-bound active centers capable of stimulating PMS activation, with $\equiv$Fe(II) generated by the rapid charge transfer of nZVI and $\equiv$Ti(III) existing in the Ti$_3$C$_2$-based MXene lattice. EPR results indicated that SO$_4^{\cdot-}$ and HO$^{\cdot}$ were the main products formed after PMS activation, with radical quenching experiments further confirming that SO$_4^{\cdot-}$ was the most important active oxidation species for ranitidine removal. DFT calculations demonstrated that the PMS activation process that occurred on the bi-active surface centers of nZVIPs@Ti$_3$C$_2$ nanosheets and the subsequent PMS dissociation were thermodynamically favorable. Overall, this study established a recyclable Fenton-like oxidation process for the rapid removal of ranitidine and provides novel insights into PMS molecule activation by surface bi-active centers instead of dissolved transition metal ions as the catalytic oxidation reaction centers, indicating its potential as a promising and recyclable Fenton-like oxidation process for the degradation of other challenging pollutants.

Conflicts of interest

There are no conflicts to declare.

Acknowledgements

References

1 M. Huerta-Fontela, M. T. Galceran and F. Ventura, Occurrence and removal of pharmaceuticals and hormones through drinking water treatment, *Water Res.*, 2011, **45**, 1432–1442, DOI: 10.1016/j.watres.2010.10.036.

2 Y. Wang, J. Ma, J. Zhu, Y. Ning, X. Zhang and H. Huang, Multi-walled carbon nanotubes with selected properties for dynamic filtration of pharmaceuticals and personal care products, *Water Res.*, 2016, **92**, 104–112, DOI: 10.1016/j.watres.2016.01.038.

3 M. E. Dasenaki and N. S. Thomaidis, Multianalyte method for the determination of pharmaceuticals in wastewater samples using solid-phase extraction and liquid chromatography-tandem mass spectrometry, *Anal. Bioanal. Chem.*, 2015, **407**, 4229–4245, DOI: 10.1007/s00216-015-8654-x.

4 M. Selbes, D. Kim, N. Ates and T. Karanfil, The roles of tertiary amine structure, background organic matter and chloramine species on NDMA formation, *Water Res.*, 2013, **47**, 945–953, DOI: 10.1016/j.watres.2012.11.014.

5 J. Rivas, O. Gimeno, A. Encinas and F. Beltrán, Ozonation of the pharmaceutical compound ranitidine: reactivity and kinetic aspects, *Chemosphere*, 2009, **76**, 651–656, DOI: 10.1016/j.chemosphere.2009.04.028.

6 R. Shen and S. A. Andrews, Demonstration of 20 pharmaceuticals and personal care products (PPCPs) as nitrosamine precursors during chloramine disinfection, *Water Res.*, 2010, **45**, 944–952, DOI: 10.1016/j.watres.2010.09.036.

7 J. Lv, L. Wang and Y. M. Li, Characterization of N-nitrosodimethylamine formation from the ozonation of ranitidine, *J. Environ. Sci.*, 2017, **58**, 116–126, DOI: 10.1016/j.jes.2017.05.028.

8 Y. Valcárcel, S. González-Alonso, J. L. Rodríguez-Gil, A. Gil and M. Catalzá, Detection of pharmaceutically active compounds in the rivers and tap water of the Madrid region (Spain) and potential ecotoxicological risk, *Chemosphere*, 2011, **84**, 1336–1348, DOI: 10.1016/j.chemosphere.2011.05.014.

9 F. Duarte, F. J. Maldonado-Hodar and L. M. Madeira, Influence of the particles size of activated carbons on their performance as Fe supports for developing Fenton-like catalysts, *Ind. Eng. Chem. Res.*, 2015, **51**, 9218–9226, DOI: 10.1021/ie300167r.

10 H. Xu, T. Shi, H. Zhao, L. Jin, F. Wang and S. Qi, Heterogeneous Fenton-lke discoloration of methyl orange using Fe$_3$O$_4$/MWCNTs as catalyst: process optimization by response surface methodology, *Front. Mater. Sci.*, 2016, **10**, 45–55, DOI: 10.1007/s11706-016-0324-z.

11 B. Palanivel and A. Mani, Conversion of a type-II to a z-scheme heterojunction by intercalation of a 0D electron mediator between the integrative NiFe$_2$O$_4$/g-C$_3$N$_4$ composite nanoparticles: boosting the radical production for photo-Fenton degradation, *ACS Omega*, 2020, **5**, 19747–19759, DOI: 10.1021/acsomeg.0c02477.

12 B. Palanivel, S. D. M. Perumal, T. Maiyalagan, V. Jayarman, C. Ayyappan and M. Alagiri, Rational design of ZnFe$_2$O$_4$/g-C$_3$N$_4$ nanocomposite for enhanced photo-Fenton reaction and supercapacitor performance, *Appl. Surf. Sci.*, 2019, **498**, 143807, DOI: 10.1016/j.apsusc.2019.143807.

13 S. Yang, P. Wu, J. Liu, M. Chen, Z. Ahmed and N. Zhu, Efficient removal of bisphenol A by superoxide radical and singlet oxygen generated from peroxymonosulfate activated with Fe^0-montmorillonite, *Chem. Eng. J.*, 2018, **350**, 484–495, DOI: 10.1016/j.cej.2018.04.175.

14 J. Q. Li, M. T. Li, H. Q. Sun, Z. M. Ao, S. B. Wang and S. M. Liu, Understanding of the oxidation behavior of benzyl alcohol by peroxymonosulfate via carbon nanotubes activation, *ACS Catal.*, 2020, **10**, 3516–3525, DOI: 10.1021/acscatal.9b05273.

15 J. Deng, Y. Shao, N. Gao, C. Tan, S. Zhou and X. Hu, CoFe$_2$O$_4$ magnetic nanoparticles as a highly active heterogeneous catalyst of oxone for the degradation of diclofenac in

19830 | *J. Mater. Chem. A*, 2021, **9**, 19817–19833

This journal is © The Royal Society of Chemistry 2021

water, *J. Hazard. Mater.*, 2013, **262**, 836–844, DOI: 10.1016/j.jhazmat.2013.09.049.

16 R. Zhang, P. Sun, T. H. Boyer, L. Zhao and C. H. Huang, Degradation of pharmaceuticals and metabolite in synthetic human urine by UV, UV/H$_2$O$_2$, and UV/PDS, *Environ. Sci. Technol.*, 2015, **49**, 3056–3066, DOI: 10.1021/es504799n.

17 Z. Jing, J. Ma, L. W. Chen, X. C. Li, Y. H. Guan, P. C. Xie and C. Pan, Rapid acceleration of ferrous iron/peroxymonosulfate oxidation of organic pollutants by promoting Fe(III)/Fe(II) cycle with hydroxylamine, *Environ. Sci. Technol.*, 2013, **47**, 11685–11691, DOI: 10.1021/es4019145.

18 F. Ghanbari and M. Moradi, Application of peroxymonosulfate and its activation methods for degradation of environmental organic pollutants: review, *Chem. Eng. J.*, 2017, **310**, 41–62, DOI: 10.1016/j.cej.2016.10.064.

19 A. Babuponnusami and K. Muthukumar, Removal of phenol by heterogeneous photo electro Fenton-like process using nano-zero valent iron, *Sep. Purif. Technol.*, 2012, **98**, 130–135, DOI: 10.1016/j.seppur.2012.04.034.

20 Y. Y. Ma, F. S. Meng, Y. Y. Wang, X. F. Lv and Q. Yang, Enhanced heterogeneous catalytic oxidation of 2,4-dichlorophenoxyacetic acid in aqueous solution by nanoscale zero-valent iron particles @superticlefur/nitrogen dual-doped r-GO (nZVIPs@SN-G) composites, *Appl. Catal., A*, 2018, **566**, 60–73, DOI: 10.1016/j.apcata.2018.08.013.

21 Y. Y. Ma, X. F. Lv, D. B. Xiong, X. S. Zhao and Z. H. Zhang, Catalytic degradation of ranitidine using novel magnetic Ti$_3$C$_2$-based MXene nanosheets modified with nanoscale zero-valent iron particles, *Appl. Catal., B*, 2021, **284**, 119720, DOI: 10.1016/j.apcatb.2020.119720.

22 J. T. Nurmi, P. G. Tratnyek, V. Sarathy, D. R. Baer, J. E. Amonette and K. Pecher, Characterization and properties of metallic iron nanoparticles: spectroscopy, electrochemistry, and kinetics, *Environ. Sci. Technol.*, 2005, **39**, 1221–1230, DOI: 10.1021/es049190u.

23 T. Phenrat, N. Saleh, K. Sirk, R. D. Tilton and G. V. Lowry, Aggregation and sedimentation of aqueous nanoscale zerovalent iron dispersions, *Environ. Sci. Technol.*, 2007, **41**, 284–290, DOI: 10.1021/es061349a.

24 A. Rastogi, S. R. Al-Abed and D. D. Dionysiou, Sulfate radical-based ferrous-peroxymonosulfate oxidative system for PCBs degradation in aqueous and sediment systems, *Appl. Catal., B*, 2009, **85**, 171–179, DOI: 10.1016/j.apcatb.2008.07.010.

25 Y. X. Wang, H. Q. Sun, X. G. Duan, H. M. Ang, M. O. Tadé and S. B. Wang, A new magnetic nano zero-valent iron encapsulated in carbon spheres for oxidative degradation of phenol, *Appl. Catal., B*, 2015, **172–173**, 73–81, DOI: 10.1016/j.apcatb.2015.02.016.

26 X. J. Hou, X. P. Huang, F. L. Jia, J. C. Zhao and L. Z. Zhang, Hydroxylamine promoted goethite surface Fenton degradation of organic pollutants, *Environ. Sci. Technol.*, 2017, **51**, 5118–5126, DOI: 10.1021/acs.est.6b05906.

27 Y. Wang, H. Zhao, M. Li, J. Q. Fan and G. H. Zhao, Magnetic ordered mesoporous copper ferrite as a heterogeneous Fenton catalyst for the degradation of imidacloprid, *Appl. Catal., B*, 2014, **147**, 534–545, DOI: 10.1016/j.apcatb.2013.09.017.

28 X. P. Huang, X. J. Hou, J. C. Zhao and L. Z. Zhang, Hematite facet confined ferrous ions as high efficient Fenton catalyst to degrade organic contaminants by lowering H$_2$O$_2$ decomposition energetic span, *Appl. Catal., B*, 2016, **181**, 127–137, DOI: 10.1016/j.apcatb.2015.06.061.

29 O. Mastalir, M. Naguib, V. N. Mochalin, Y. Dall-Agnese, M. Heon, M. W. Barsoum and Y. Gogotsi, Intercalation and delamination of layered carbides and carbonitrides, *Nat. Commun.*, 2013, **4**, 1716, DOI: 10.1038/ncomms2664.

30 H. Wang, Y. Wu, X. Yuan, G. M. Zeng, J. Zhou, X. Wang and J. W. Chew, Clay-inspired MXene-based electrochemical devices and photo-electrocatalyst: state-of-the-art progresses and challenges, *Adv. Mater.*, 2018, **30**, 1704561, DOI: 10.1002/adma.201704561.

31 L. Jiao, C. Zhang, C. N. Geng, S. C. Wu, H. Li, W. Lv, Y. Tao, Z. J. Chen, G. M. Zhou and J. Li, Capture and catalytic conversion of polysulfides by in situ built TiO$_2$-MXene heterostructures for lithium-sulfur batteries, *Adv. Energy Mater.*, 2019, **9**, 1900219.1–1900219.9, DOI: 10.1002/aenm.201900219.

32 H. Huang, Y. Song, N. J. Li, D. Y. Chen, Q. F. Xu, H. Li, J. H. He and J. M. Lu, One-step in situ preparation of N-doped TiO$_2$@C derived from Ti$_3$C$_2$ MXene for enhanced visible-light driven photodegradation, *Appl. Catal., B*, 2019, **251**, 154–161, DOI: 10.1016/j.apcatb.2019.03.066.

33 C. Christophoridis, M. C. Nika, R. Aalizadeh and N. S. Thomaidis, Ozonation of ranitidine: effect of experimental parameters and identification of transformation products, *Sci. Total Environ.*, 2016, **556–558**, 170–182, DOI: 10.1016/j.scitotenv.2016.03.026.

34 A. S. Mohamed, F. Olfat, A. A. Shaeel and O. Y. Abdullah, Removal of nitrate ions from aqueous solution using zero-valent iron nanoparticles supported on high surface area nanographenes, *J. Mol. Liq.*, 2015, **212**, 708–715, DOI: 10.1016/j.molliq.2015.09.029.

35 F. F. Wang, Y. Wu, Y. Gao, H. Li and Z. L. Chen, Effect of humic acid, oxalate and phosphate on Fenton-like oxidation of microcystin-LR by nanoscale zero-valent iron, *Sep. Purif. Technol.*, 2016, **170**, 337–343, DOI: 10.1016/j.seppur.2016.06.046.

36 D. Li, Y. Y. Wei, Y. J. Wang, H. B. Chen, J. Caro and H. H. Wang, A two-dimensional lamellar membrane: MXene nanosheet stacks, *Angew. Chem., Int. Ed.*, 2017, **129**, 1–6, DOI: 10.1002/anie.201609306.

37 M. Naguib, M. Kurtoglu, V. Presser, J. Liu, J. Niu, M. Heon, L. Hultman, Y. Gogotsi and M. W. Barsoum, Two-dimensional nanocrystals produced by exfoliation of Ti$_3$AlC$_2$, *Adv. Mater.*, 2011, **23**, 4248–4253, DOI: 10.1002/adma.201102306.

38 L. J. Xu and J. L. Wang, Magnetic nanoscaled Fe$_3$O$_4$/CeO$_2$ composite as an efficient Fenton-like heterogeneous

This journal is © The Royal Society of Chemistry 2021

J. Mater. Chem. A, 2021, **9**, 19817–19833 | **19831**

catalyst for degradation of 4-Chlorophenol, *Environ. Sci. Technol.*, 2012, **46**, 10145–10153, DOI: 10.1021/es300303f.

39 F. Duarte, F. J. Maldonado-Hódar, A. F. Pérez-Cadenas and L. M. Madeira, Fenton-like degradation of azo-dye orange II catalyzed by transition metals on carbon aerogels, *Appl. Catal., B*, 2009, **85**, 139–147, DOI: 10.1016/j.apcatb.2008.07.006.

40 S. Agarwal, I. Tyagi, V. K. Gupta, M. Dastkhoon, M. Ghaedi, F. Yousefi, *et al.*, Ultrasound-assisted adsorption of sunset yellow CFC dye onto Cu doped ZnS nanoparticles loaded on activated carbon using response surface methodology based on central composite design, *J. Mol. Liq.*, 2016, **219**, 332–340, DOI: 10.1016/j.molliq.2016.02.100.

41 S. G. Nasab, A. Teimouri, M. J. Yazd, T. M. Isfahani and S. Habibollahi, Decolorization of crystal violet from aqueous solutions by a novel adsorbent chitosan/nanodiopside using response surface methodology and artificial neural network-genetic algorithm, *Int. J. Biol. Macromol.*, 2019, **124**, 429–443, DOI: 10.1016/j.ijbiomac.2018.11.148.

42 T. S. B. Abd Manan, T. Khan, S. Sivapalan, H. Jusoh, N. Sapari, A. Sarwono, *et al.*, Application of response surface methodology for the optimization of polycyclic aromatic hydrocarbons degradation from potable water using photo-Fenton oxidation process, *Sci. Total Environ.*, 2019, **665**, 196–212, DOI: 10.1016/j.scitotenv.2019.02.060.

43 J. R. Domínguez, T. González, P. Palo and E. M. Cuerda-Correa, Fenton + Fenton-like integrated process for carbamazepine degradation: optimizing the system, *Ind. Eng. Chem. Res.*, 2012, **51**, 2531–2538, DOI: 10.1021/ie201980p.

44 L. H. Wang, J. Jiang, S. Y. Pang, Y. Zhou, J. Li, S. F. Sun, *et al.*, Oxidation of bisphenol A by nonradical activation of peroxymonosulfate in the presence of amorphous manganese dioxide, *Chem. Eng. J.*, 2018, **352**, 1004–1013, DOI: 10.1016/j.cej.2018.07.103.

45 S. L. Wang, J. F. Wu, X. Q. Lu, W. X. Xu, Q. Gong, J. Q. Ding, *et al.*, Removal of acetaminophen in the Fe^{2+}/persulfate system: kinetic model and degradation pathways, *Chem. Eng. J.*, 2019, **358**, 1091–1100, DOI: 10.1016/j.cej.2018.09.145.

46 S. Daneshgar, P. A. Vanrolleghem, C. Vaneeckhaute, A. Buttafava and A. G. Capodaglio, Optimization of p compounds recovery from aerobic sludge by chemical modeling and response surface methodology combination, *Sci. Total Environ.*, 2019, **668**, 668–677, DOI: 10.1016/j.scitotenv.2019.03.055.

47 W. Song, J. Li, Z. Wang, C. Fu, X. Zhang, J. Feng, Z. Xu and Q. Song, Degradation of bisphenol A by persulfate coupled with dithionite: optimization using response surface methodology and pathway, *Sci. Total Environ.*, 2020, **699**, 124258, DOI: 10.1016/j.scitotenv.2019.134258.

48 R. V. Muralidhar, R. R. Chirumamila, R. Marchant and P. Nigam, A response surface approach for the comparison of lipase production by candida cylindracea using two different carbon sources, *Biochem. Eng. J.*, 2001, **9**, 17–23, DOI: 10.1016/S1369-703X(01)00117-6.

49 W. Hayat, Y. Q. Zhang, I. Hussain, X. D. Du, M. M. Du, C. H. Yao, S. B. Huang and F. Si, Efficient degradation of imidacloprid in water through iron activated sodium persulfate, *Chem. Eng. J.*, 2019, **370**, 1169–1180, DOI: 10.1016/j.cej.2019.03.261.

50 Y. G. Kang, H. C. Vu, T. T. Le and Y. S. Chang, Activation of persulfate by a novel Fe(II)-immobilized chitosan/alginate composite for bisphenol A degradation, *Chem. Eng. J.*, 2018, **353**, 736–745, DOI: 10.1016/j.cej.2018.07.175.

51 S. Xiao, M. Cheng, H. Zhong, Z. F. Liu, Y. Liu, X. Yang and Q. H. Liang, Iron-mediated activation of persulfate and peroxymonosulfate in both homogeneous and heterogeneous ways: a review, *Chem. Eng. J.*, 2020, **384**, 123265, DOI: 10.1016/j.cej.2019.123265.

52 C. Liu, L. Y. Liu, X. Tian, Y. P. Wang, R. Y. Li, Y. T. Zhang, Z. L. Song, B. B. Xu, W. Chu, F. Qi and A. Ikhlaq, Coupling metal-organic frameworks and g-C_3N_4 to derive Fe@N-doped graphene-like carbon for peroxymonosulfate activation: upgrading framework stability and performance, *Appl. Catal., B*, 2019, **255**, 11, DOI: 10.1016/j.apcatb.2019.117763.

53 Y. H. Guan, J. Ma, Y. M. Ren, Y. L. Liu, J. Y. Xiao, L. Q. Lin and C. Zhang, Efficient degradation of atrazine by magnetic porous copper ferrite catalyzed peroxymonosulfate oxidation via the formation of hydroxyl and sulfate radicals, *Water Res.*, 2013, **47**, 5431–5438, DOI: 10.1016/j.watres.2013.06.023.

54 J. Li, Q. Liu, Q. Q. Ji and B. Lai, Degradation of p-nitrophenol (PNP) in aqueous solution by Fe-0-PM-PS system through response surface methodology (RSM), *Appl. Catal., B*, 2017, **200**, 633–646, DOI: 10.1016/j.apcatb.2016.07.026.

55 J. Li, M. J. Xu, G. Yao and B. Lai, Enhancement of the degradation of atrazine through $CoFe_2O_4$ activated peroxymonosulfate (PMS) process: kinetic, degradation intermediates, and toxicity evaluation, *Chem. Eng. J.*, 2018, **348**, 1012–1024, DOI: 10.1016/j.cej.2018.05.032.

56 M. J. Xu, J. Li, Y. Yan, X. G. Zhao, J. F. Yang, Y. H. Zhang, B. Lai, X. Chen and L. P. Song, Catalytic degradation of sulfamethoxazole through peroxymonosulfate activated with expanded graphite loaded $CoFe_2O_4$ particles, *Chem. Eng. J.*, 2019, **369**, 403–413, DOI: 10.1016/j.cej.2019.03.075.

57 W. Yan, A. A. Herzing, C. J. Kiely and W. X. Zhang, Nanoscale zero-valent iron (nZVI): aspects of the core-shell structure and reactions with inorganic species in water, *J. Contam. Hydrol.*, 2010, **118**, 96–104, DOI: 10.1016/j.jconhyd.2010.09.003.

58 A. Jawad, J. Lang, Z. W. Liao, A. Khan, J. Ifthikar, Z. N. Lv, S. J. Long, Z. L. Chen and Z. Q. Chen, Activation of persulfate by CuO_x@Co-LDH: a novel heterogeneous system for contaminant degradation with broad pH window and controlled leaching, *Chem. Eng. J.*, 2018, **335**, 548–559, DOI: 10.1016/j.cej.2017.10.097.

59 Y. Feng, D. Wu, Y. Deng, T. Zhang and K. Shih, Sulfate radical-mediated degradation of sulfadiazine by $CuFeO_2$ rhombohedral crystal-catalyzed peroxymonosulfate: synergistic effects and mechanisms, *Environ. Sci. Technol.*, 2016, **50**, 3119–3127, DOI: 10.1021/acs.est.5b05974.

19832 | *J. Mater. Chem. A*, 2021, **9**, 19817–19833

This journal is © The Royal Society of Chemistry 2021

60 W. Z. Yin, J. H. Wu, P. Li, X. D. Wang, N. W. Zhu, P. X. Wu and B. Yang, Experimental study of zero-valent iron induced nitrobenzene reduction in groundwater: the effects of pH, iron dosage, oxygen and common dissolved anions, *Chem. Eng. J.*, 2012, **184**, 198–204, DOI: 10.1016/j.cej.2012.01.030.

61 Y. Yang, J. J. Pignatello, J. Ma and W. A. Mitch, Comparison of halide impacts on the efficiency of contaminant degradation by sulfate and hydroxyl radical-based advanced oxidation processes (AOPs), *Environ. Sci. Technol.*, 2014, **48**, 2344–2351, DOI: 10.1021/es404118q.

62 L. Chen, S. Yang, X. Zuo, Y. Huang, T. Cai and D. Ding, Biochar modification significantly promotes the activity of Co_3O_4 towards heterogeneous activation of peroxymonosulfate, *Chem. Eng. J.*, 2018, **354**, 856–865, DOI: 10.1016/j.cej.2018.08.098.

63 P. Hu and M. Long, Cobalt-catalyzed sulfate radical-based advanced oxidation: a review on heterogeneous catalysts and applications, *Appl. Catal., B*, 2016, **181**, 103–117, DOI: 10.1016/j.apcatb.2015.07.024.

64 X. Duan, Z. Ao, L. Zhou, H. Sun, G. Wang and S. Wang, Occurrence of radical and nonradical pathways from carbocatalysts for aqueous and nonaqueous catalytic oxidation, *Appl. Catal., B*, 2016, **188**, 98–105, DOI: 10.1016/j.apcatb.2015.07.024.

65 G. Baril and N. Pébère, The corrosion of pure magnesium in aerated and deaerated sodium sulphate solutions, *Corros. Sci.*, 2001, **43**, 471–484, DOI: 10.1016/S0010-938X(00)00095-0.

66 H. Li, J. Tian, Z. Zhu, F. Cui, Y. A. Zhu, X. Duan and S. Wang, Magnetic nitrogen-doped nanocarbons for enhanced metal-free catalytic oxidation: integrated experimental and theoretical investigations for mechanism and application, *Chem. Eng. J.*, 2018, **354**, 507–516, DOI: 10.1016/j.cej.2018.08.043.

67 M. Xie, J. Tang, L. Kong, W. Lu, V. Natarajan, F. Zhu and J. Zhan, Cobalt doped g-C_3N_4 activation of peroxymonosulfate for monochlorophenols degradation, *Chem. Eng. J.*, 2019, **360**, 1213–1222, DOI: 10.1016/j.cej.2018.10.130.

68 K. K. Xiao, J. Wang, Z. Chen, Y. H. Qian, Z. Liu, L. L. Zhang, X. H. Chen, J. L. Liu, X. F. Fan and Z. X. Shen, Improving polysulfides adsorption and redox kinetics by the Co_4N nanoparticles/N-doped carbon composites for lithium-sulfur batteries, *Small*, 2019, **15**, 1901454, DOI: 10.1002/smll.201901454.

69 D. B. Xiong, X. F. Li, H. Shan, B. Yan, L. T. Dong, Y. Cao and D. J. Li, Controllable oxygenic functional groups of metal-free cathodes for high performance lithium ion batteries, *J. Mater. Chem. A*, 2015, **3**, 11376–11386, DOI: 10.1039/c5ta01574j.

70 T. Zeng, X. L. Zhang, S. H. Wang, H. Y. Niu and Y. Q. Cai, Spatial confinement of a Co_3O_4 catalyst in hollow metal-organic framework as a nanoreactor for improved degradation of organic pollutants, *Environ. Sci. Technol.*, 2015, **49**, 2350–2357, DOI: 10.1021/es505014z.

71 W. D. Oh, Z. Dong and T. T. Lim, Generation of sulfate radical through heterogeneous catalysis for organic contaminants removal: current development, challenges and prospects, *Appl. Catal., B*, 2016, **194**, 169–201, DOI: 10.1016/j.apcatb.2016.04.003.

72 G. X. Huang, C. Y. Wang, C. W. Yang, P. C. Guo and H. Q. Yu, Degradation of bisphenol A by peroxymonosulfate catalytically activated with $Mn_{1.8}Fe_{1.2}O_4$ nanospheres: synergism between Mn and Fe, *Environ. Sci. Technol.*, 2017, **51**, 12611–12618, DOI: 10.1021/acs.est.7b03007.

73 X. Duan, Z. Ao, H. Zhang, M. Saunders, H. Sun, Z. Shao and S. Wang, Nanodiamonds in sp^2/sp^3 configuration for radical to nonradical oxidation: core-shell layer dependence, *Appl. Catal., B*, 2018, **222**, 176–181, DOI: 10.1016/j.apcatb.2017.10.007.

74 Q. G. Jiang, M. Z. Ao, S. Li and Z. Wen, Density functional theory calculations on the CO catalytic oxidation on Al-embedded graphene, *RSC Adv.*, 2014, **4**, 20290–20296, DOI: 10.1039/c4ra01908c.

75 J. Liu, J. H. Zhou, Z. X. Ding, Z. W. Zhao, X. Xu and Z. D. Fang, Ultrasound irritation enhanced heterogeneous activation of peroxymonosulfate with Fe_3O_4 for degradation of azo dye, *Ultrason. Sonochem.*, 2017, **34**, 953–959, DOI: 10.1016/j.ultsonch.2016.08.005.

76 H. Zheng, J. G. Bao, Y. Huang, L. J. Xiang, Faheem, B. X. Ren, J. K. Du, M. N. Nadagouda and D. D. Dionysiou, Efficient degradation of atrazine with porous sulfurized Fe_2O_3 as catalyst for peroxymonosulfate activation, *Appl. Catal., B*, 2019, **259**, 118056, DOI: 10.1016/j.apcatb.2019.118056.

This journal is © The Royal Society of Chemistry 2021

J. Mater. Chem. A, 2021, **9**, 19817–19833 | **19833**